nature communications

Article

https://doi.org/10.1038/s41467-024-52621-x

Lipid droplets sequester palmitic acid to disrupt endothelial ciliation and exacerbate atherosclerosis in male mice

Received: 27 March 2024

Accepted: 17 September 2024

Published online: 27 September 2024

Check for updates

Yanjie Tan[1,8], Zhenzhou Huang[1,8], Yi Jin[2], Jiaying Wang[1], Hongjun Fan[1], Yangyang Liu[1], Liang Zhang[2], Yue Wu[1], Peiwei Liu[1], Tianliang Li[1], Jie Ran[1], He Tian[3], Sin Man Lam[3,4], Min Liu[5], Jun Zhou[1,6] ✉ & Yunfan Yang[7] ✉

Disruption of ciliary homeostasis in vascular endothelial cells has been implicated in the development of atherosclerosis. However, the molecular basis for the regulation of endothelial cilia during atherosclerosis remains poorly understood. Herein, we provide evidence in male mice that the accumulation of lipid droplets in vascular endothelial cells induces ciliary loss and contributes to atherosclerosis. Triglyceride accumulation in vascular endothelial cells differentially affects the abundance of free fatty acid species in the cytosol, leading to stimulated lipid droplet formation and suppressed protein S-palmitoylation. Reduced S-palmitoylation of ciliary proteins, including ADP ribosylation factor like GTPase 13B, results in the loss of cilia. Restoring palmitic acid availability, either through pharmacological inhibition of stearoyl-CoA desaturase 1 or a palmitic acid-enriched diet, significantly restores endothelial cilia and mitigates the progression of atherosclerosis. These findings thus uncover a previously unrecognized role of lipid droplets in regulating ciliary homeostasis and provide a feasible intervention strategy for preventing and treating atherosclerosis.

Atherosclerosis continues to be one of the leading causes of morbidity and mortality globally and remains the most frequent underlying pathology of cardiovascular diseases, including coronary artery disease, peripheral artery disease, and cerebrovascular disease[1]. The chronic accumulation of vessel-occluding plaques in the subendothelial intimal layer of large and medium-sized arteries eventually leads to significant stenosis, restricting blood flow and causing critical tissue hypoxia[2]. Its most common complications include myocardial infarction, stroke, and peripheral vascular disease[3,4]. While some antihyperlipidemic drugs are widely used for the treatment and prevention of cardiovascular disease, their use is limited due to the presence of unpleasant side effects. Therefore, alternative strategies, such as lifestyle changes, have been proposed as potential solutions to this problem. However, effective interventions, such as exercise and dietary management, may be challenging to implement. In addition, the efficacy and detailed mechanisms of these interventions remain insufficiently understood, which seriously limits the development of more effective strategies.

[1]Center for Cell Structure and Function, Haihe Laboratory of Cell Ecosystem, Collaborative Innovation Center of Cell Biology in Universities of Shandong, Shandong Provincial Key Laboratory of Animal Resistance Biology, College of Life Sciences, Shandong Normal University, 250014 Jinan, China. [2]Metabolism and Disease Research Centre, Central Hospital Affiliated to Shandong First Medical University, 250013 Jinan, China. [3]State Key Laboratory of Molecular Developmental Biology, Institute of Genetics and Developmental Biology, Chinese Academy of Sciences, 100101 Beijing, China. [4]LipidALL Technologies Company Limited, 213022 Changzhou, China. [5]Laboratory of Tissue Homeostasis, Haihe Laboratory of Cell Ecosystem, 300462 Tianjin, China. [6]State Key Laboratory of Medicinal Chemical Biology, College of Life Sciences, Nankai University, 300071 Tianjin, China. [7]Department of Cell Biology, School of Basic Medical Sciences, Cheeloo College of Medicine, Shandong University, 250012 Jinan, China. [8]These authors contributed equally: Yanjie Tan, Zhenzhou Huang. ✉e-mail: junzhou@sdnu.edu.cn; yunfanyang@sdu.edu.cn

Under normal conditions, vascular endothelial cells (VECs) are able to sustain vascular homeostasis and inhibit atherosclerosis by regulating vascular tension, preventing thrombosis, and suppressing inflammation[5]. Damage to VECs is commonly regarded as a key early event in the pathogenesis of atherosclerosis[6]. Persistent and extensive endothelial damage impairs vascular integrity and reduces vascular barrier function, facilitating the deposition of lipids and monocytes in the intima, thereby promoting the formation of foam cells and atherosclerotic plaques, and accelerating the onset of atherosclerosis[7]. Atherosclerotic plaques are predominantly found in high curvature regions and branching points of the aorta, coinciding with the enrichment of primary cilia, which are hair-like microtubule-based structures that extend into the vascular lumen[8–11]. Previous studies have demonstrated that endothelial cilia serve as molecular switches for calcium ions and nitric oxide signaling, thus contributing to essential vascular functions[12–14]. Additionally, endothelial cilia function as mechanosensors to monitor blood flow[12,15,16]. Dysregulation of this process results in aberrant fluid perception, which in turn contributes to vascular diseases by promoting VEC epithelial-mesenchymal transition[17–20]. Using a genetic mouse model with endothelial cilia deficiency, a previous study demonstrated that the absence of cilia accelerates the development of atherosclerosis[8]. Therefore, a further understanding of the upstream mechanism underlying the loss of epithelial cilia during the early stage of atherosclerosis may provide opportunities for the development of preventative and therapeutic strategies for atherosclerosis.

VECs are constantly exposed to cycles of lipid fluctuations from dietary fats and lipoproteins[21]. A balanced lipid metabolism is critical for maintaining intracellular homeostasis in VECs[22]. Accumulating evidence has shown that lipid droplets (LDs), where fatty acids are stored in the form of triglycerides, serve as the hub of intracellular lipid metabolism to dynamically adjust fatty acid flux in VECs[21,23]. In response to a postprandial surge of excess fatty acids, cells upregulate the esterification of fatty acids and store them within LDs[24]. When external fatty acids are scarce, fatty acids can be released from LDs through lipolysis and utilized for energy production and cellular lipid synthesis[25,26]. Stressful conditions, such as overnutrition, disrupt lipid metabolism and the balance between LD synthesis and catabolism in VECs, which ultimately results in vascular endothelial dysfunction[21]. In addition to maintaining lipid metabolism and energy homeostasis, LDs, like other organelles, are complex, active and dynamic. They play essential roles in membrane transport, protein degradation, signal transduction, and even the regulation of gene expression. LDs can also modulate the functions of other organelles, such as the endoplasmic reticulum (ER), mitochondria, and peroxisomes, by directly interacting with them and facilitating the inter-organelle exchange of proteins and lipids[26,27]. However, there is no current knowledge on whether LDs can affect the homeostasis of cilia.

The composition and balance of dietary fatty acids play a critical role in maintaining lipid homeostasis in VECs. Stearoyl-CoA desaturase 1 (SCD1) is a crucial enzyme involved in lipid metabolism, catalyzing the conversion of saturated fatty acids to monounsaturated fatty acids, which is essential for maintaining membrane integrity and lipid homeostasis[28]. SCD1 has emerged as an attractive target for cancer therapy due to its involvement in tumor cell proliferation, survival, and metastasis[28–30]. A previous study demonstrated that exposure of C57BL/6J mice to chronic intermittent hypoxia and a high-cholesterol diet leads to the development of atherosclerosis, concomitant with an upregulation of hepatic SCD1[31]. Notably, the administration of SCD1 antisense oligonucleotides effectively mitigated atherosclerosis in the aorta of mice during exposure to chronic intermittent hypoxia[31]. However, another study has reported contrasting findings, indicating that inhibiting SCD1 using antisense oligonucleotides accelerates atherosclerosis in the $Ldlr^{KO}Apob^{100/100}$ mouse model of hyperlipidemia and atherosclerosis[32]. These findings underscore the complex role of SCD1 in metabolism and the significance of SCD1 in atherosclerosis. Further research is needed to elucidate the complex interplay between SCD1, lipid metabolism, and endothelial dysfunction in the context of atherosclerosis pathogenesis.

In the present study, we observed that mice fed with a high-fat diet (HFD) exhibited enhanced LD formation, impaired ciliation, and elevated SCD1 expression in their VECs. By further dissecting the interplay between LDs and cilia, we found that the buildup of triglycerides, acting together with elevated SCD1, tips the balance of saturated and monounsaturated fatty acids in VECs, leading to a decrease in the availability of palmitic acid (PA) and a reduction in the S-palmitoylation of ciliary proteins, including ADP ribosylation factor like GTPase 13B (ARL13B), resulting in disrupted endothelial ciliary homeostasis and exacerbated atherosclerosis. In addition, we demonstrated that the progression of HFD-induced atherosclerosis in a mouse model could be substantially mitigated by restoring PA availability through SCD1 inhibition or palm oil supplementation. Thus, our study suggests that dietary supplementation with palm oil could serve as an effective approach for the prevention and treatment of atherosclerosis.

Results

Concomitant LD accumulation and ciliary loss in VECs during atherosclerosis progression

Ablation of endothelial primary cilia has been shown to exacerbate atherosclerosis in mice[8]. To investigate the dynamics of ciliation in VECs during the progression of atherosclerosis, *apolipoprotein E* knockout ($ApoE^{KO}$) mice were fed with a HFD to induce atherosclerosis. Oil Red O (ORO) staining of the entire aorta showed that HFD-fed $ApoE^{KO}$ mice exhibited significantly increased atherosclerosis lesions (Fig. 1a, b) and aortic sinus (Supplementary Fig. 1a, b) compared to mice fed a normal chow (NC), indicating the successful establishment of the atherosclerosis mouse model. *En face* imaging of the inner curvature of the aortic arch was then utilized to examine the dynamics of endothelial primary cilia in VECs during the progression of atherosclerosis. Immunostaining of acetylated tubulin (ac-tubulin), a well-characterized marker of the ciliary axoneme, revealed a significant disruption of ciliation in VECs from mice with atherosclerosis (Fig. 1c, e and Supplementary Fig. 1c). Staining of neutral lipids with BODIPY 493/503 indicated a prominent accumulation of LDs in VECs of mice with atherosclerosis (Fig. 1c, d and Supplementary Fig. 1c). Notably, there were more LDs in nonciliated cells compared to ciliated cells (Supplementary Fig. 1d). Moreover, an analysis of ciliary signal and LD signal of VECs of the inner curvature of the aortic arch revealed that LD accumulation and ciliary loss occurred simultaneously in VECs during the progression of atherosclerosis (Fig. 1f, g and Supplementary Fig. 1e, f). These findings indicate that LD accumulation in VECs may contribute to the disruption of endothelial primary cilia as atherosclerosis progresses.

LD accumulation triggers ciliary loss in VECs

Next, we sought to determine whether the accumulation of LDs in VECs is involved in the disruption of ciliary homeostasis. LD formation was induced in cultured human aortic endothelial cells (HAECs) by supplementing monounsaturated oleic acid (OA) into the culture medium. Immunofluorescence microscopy revealed that OA dose-dependently induced an accumulation of LDs and a reduction in serum starvation-induced ciliation in HAECs (Fig. 2a–c). To further validate the effect of LD accumulation on ciliation, Atglistatin was used to block the activity of ATGL, the key lipid hydrolase initiating LD lipolysis. Immunofluorescence analysis revealed that Atglistatin treatment caused significant LD accumulation as well as a significant disruption of ciliation in HAECs (Fig. 2d–f). We further suppressed triglyceride synthesis in HUVECs by co-treatment with A922500 and PF-06424439, specific inhibitors that block diglyceride acyltransferase-1 (DGAT1) and DGAT2, respectively. This treatment almost completely abolished the

https://doi.org/10.1038/s41467-024-52621-x

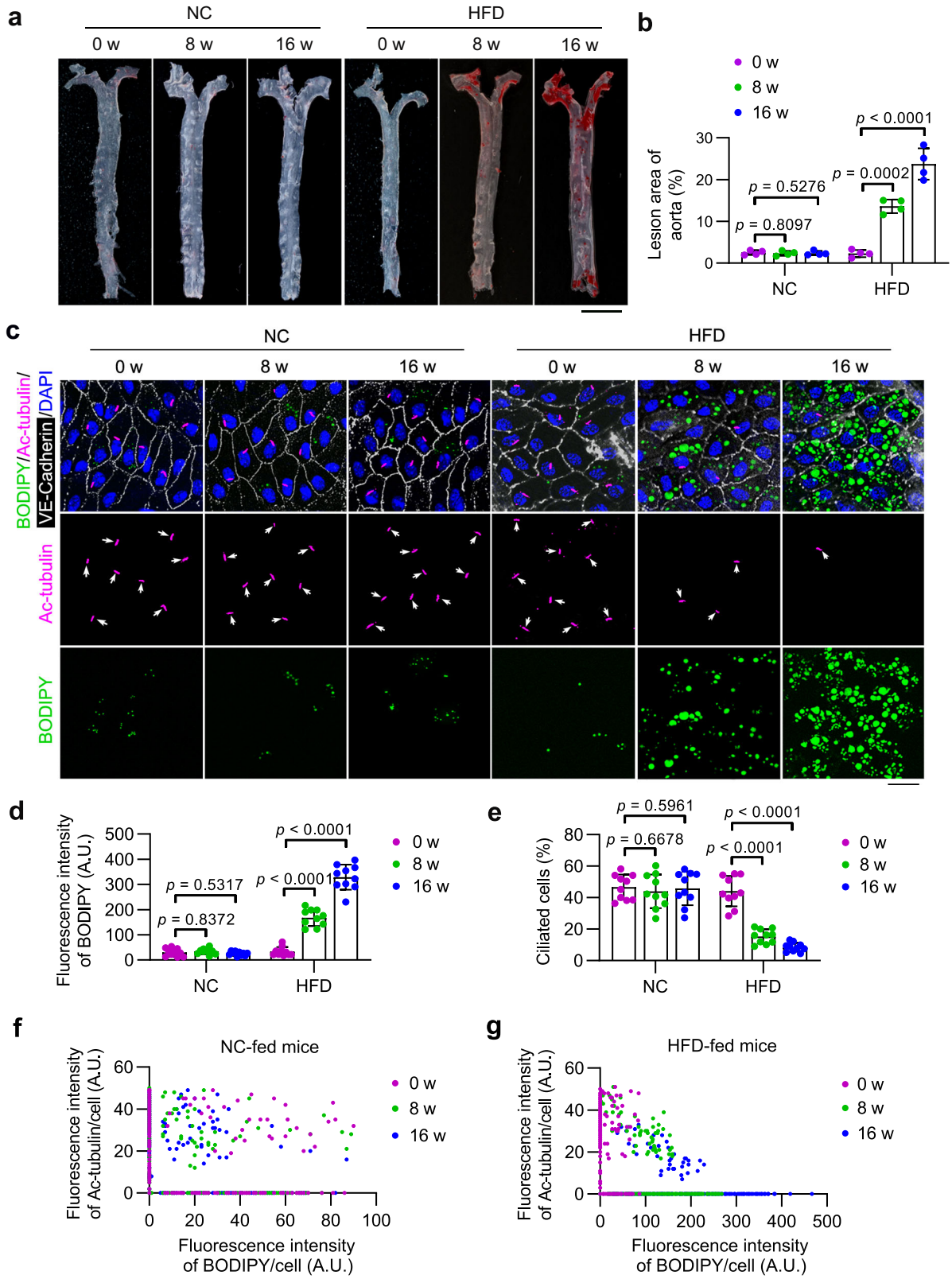

Fig. 1 | LD accumulation coincides with ciliary loss in VECs during atherosclerosis progression. a, **b** Representative ORO staining and quantitative analysis of the whole aorta from 8-week-old ApoE^{KO} mice fed a normal chow (NC) or a high-fat diet (HFD) for 0, 8, and 16 weeks ($n = 4$ mice). Scale bar, 5 mm. **c** *En face* immunofluorescence images of the inner curvature of the aortic arch VECs stained with antibodies against VE-cadherin (white) and ac-tubulin (magenta). LDs were stained with BODIPY (green), and nuclei were stained with DAPI (blue). Scale bar, 10 μm. **d**, **e** Quantification of BODIPY staining (**d**) and ciliation (**e**) of VECs of the aortic arch shown in (**c**) ($n = 10$ mice). **f**, **g** Scatter plots showing the relationship between ciliary signal and LD signal of randomly chosen ciliated VECs of the inner curvature of the aortic arch ($n = 10$ mice for each group). Male mice were used for this study. Data are presented as mean ± SEM. Statistical significance was determined by one-way ANOVA with post hoc analysis. Source data are provided as a Source Data file.

https://doi.org/10.1038/s41467-024-52621-x

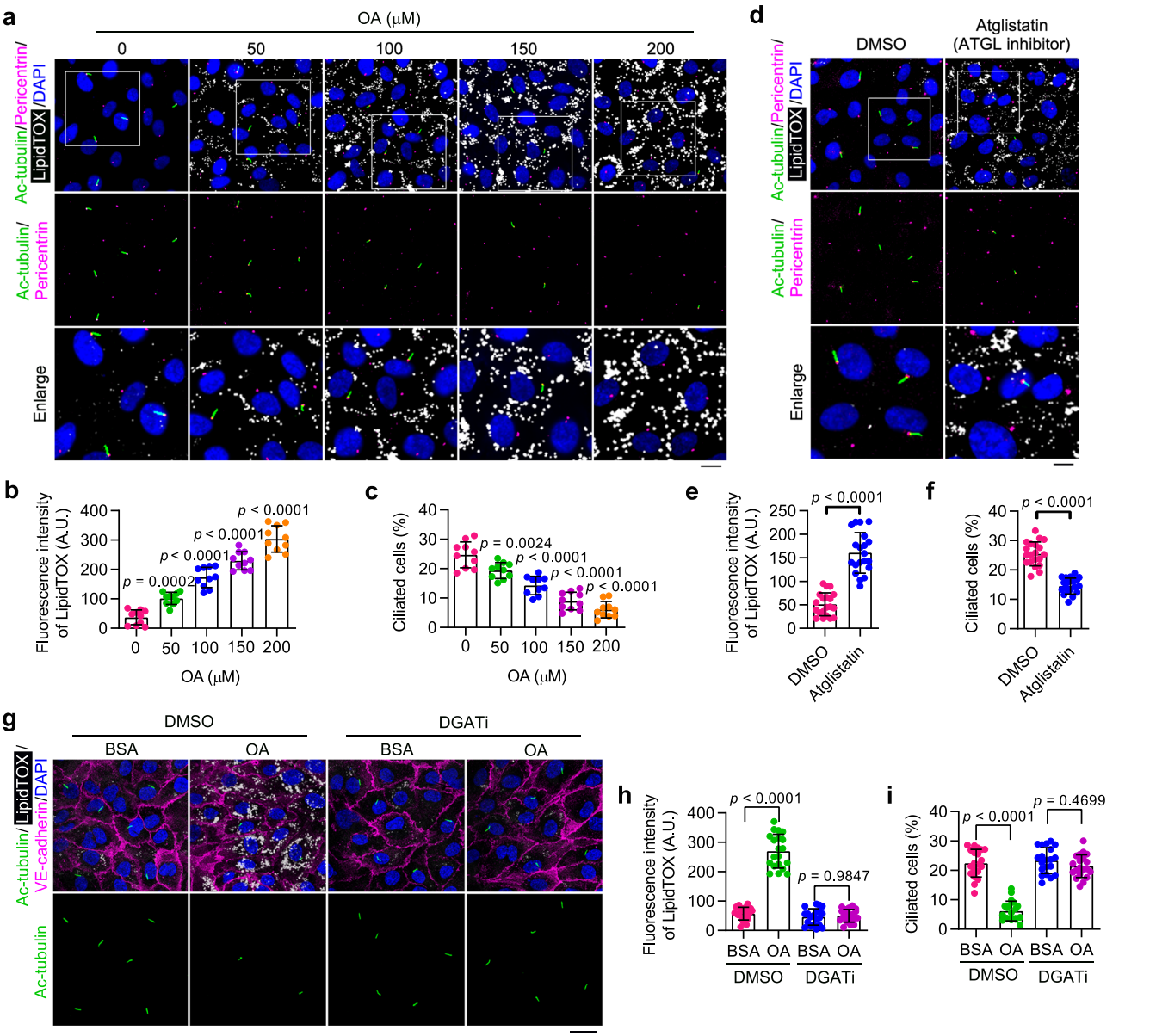

Fig. 2 | Accumulation of LDs triggers ciliary loss in cultured VECs. **a**–**c** Immunofluorescence images (**a**) and quantifications of LipidTOX staining (**b**) and ciliation (**c**) of cultured HAECs treated with oleic acid (OA) at the indicated concentration for 12 h, followed by serum starvation for 48 h ($n = 10$ fields from 3 independent experiments). Boxed areas are enlarged in the bottom panel. Scale bar (for enlarged images), 10 μm. **d**–**f** Immunofluorescence images (**d**) and quantifications of LipidTOX staining (**e**) and ciliation (**f**) of HAECs treated with ATGL inhibitor (Atglistatin, 10 μM) for 12 h, followed by serum starvation for 48 h ($n = 20$ fields from 3 independent experiments). Boxed areas are enlarged in the bottom panel. Scale bar (for enlarged images), 10 μm. **g**–**i** Immunofluorescence images (**g**) and quantifications of LipidTOX staining (**h**) and ciliation (**i**) of HAECs treated with DMSO or DGAT inhibitors (A922500, 10 μM and PF-06424439, 5 μM) for 24 h, exposed to bovine serum albumin (BSA) or OA for 12 h, and then serum-starved for 48 h ($n = 20$ fields from 3 independent experiments). 200 μM OA was used to stimulate LD formation. BSA was used as a control treatment. Scale bar, 20 μm. Data are presented as mean ± SEM. Statistical significance was determined by unpaired two-tailed Student's *t*-test (**e**, **f**), one-way (**b**, **c**), or two-way (**h**, **i**) ANOVA with post hoc analysis. Source data are provided as a Source Data file.

formation of LDs, and this was able to reverse OA-induced ciliary loss in HAECs (Fig. 2g–i). Similar results were also observed in HUVECs (Supplementary Fig. 2). Collectively, these results provide evidence that elevated triglyceride synthesis and LD accumulation contribute to the disruption of endothelial primary cilia.

Reduced PA availability is responsible for LD-associated ciliary loss

LDs have been shown to interact both functionally and physically with several other cellular organelles, and these interactions are tightly orchestrated to perform diverse functions[27]. Since LDs localize in the cytoplasm, we first determined whether LDs directly interact with the basal body, the structure located at the base of cilia. Staining with antibody against γ-tubulin (a marker of basal body/centrosome) and BODIPY 493/503 for neutral lipids showed no obvious direct contact between the basal body and LDs (Supplementary Fig. 3a).

Facilitated by fatty acid desaturases such as SCD1, unsaturated bonds can be incorporated into the carbon chain of fatty acids. Excess fatty acids can be esterified into triglycerides and stored in LDs (Fig. 3a). Notably, OA (C18:1) possesses robust triglyceride synthesis-promoting capabilities, thereby activating the pathway leading to LD biogenesis and consequently resulting in LD accumulation[33–35]. LD biogenesis and degradation are tightly coupled to cellular fatty acid metabolism, and they are critical for buffering the levels of toxic lipid species[25].

https://doi.org/10.1038/s41467-024-52621-x

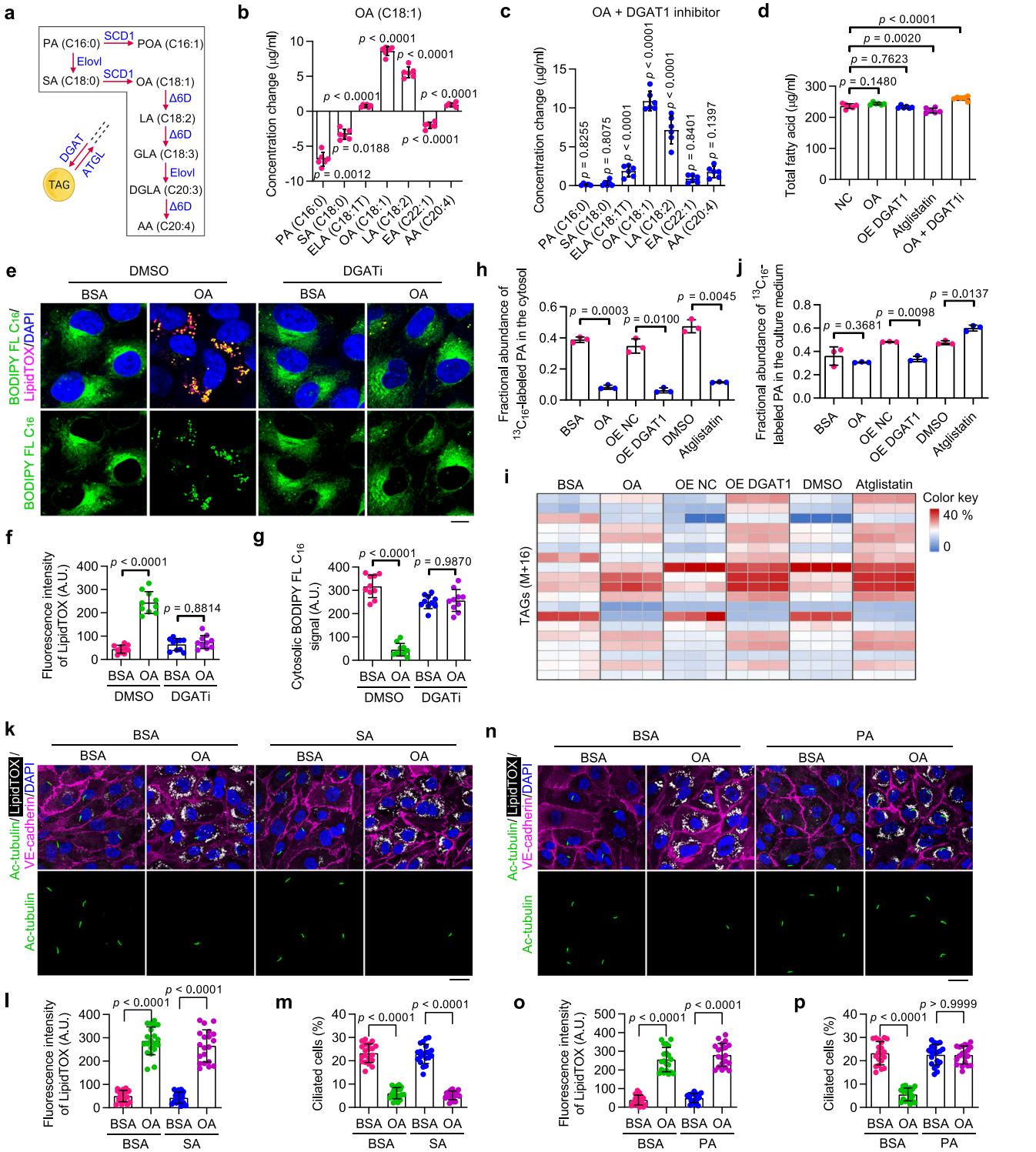

Fig. 3 | LD accumulation disrupts ciliary homeostasis by reducing cytosolic PA availability. a Metabolic pathway of indicated fatty acids. SCD1 stearoyl-CoA desaturase-1, Elovl Elongation of very long-chain fatty acid, Δ6D Δ6 desaturase, PA palmitic acid, POA palmitoleic acid, SA stearic acid, OA oleic acid, LA linoleic acid, GLA gamma-linolenic acid, DGLA dihomo-γ-linolenic acid, AA arachidonic acid. **b**, **c** GC-MS analysis showing changes in levels of indicated free fatty acids in HUVECs ($n = 6$ samples). ELA elaidic acid, EA erucic acid. **d** GC-MS analysis showing changes in the total free fatty acid level in HUVECs ($n = 6$ samples). **e**–**g** Immunofluorescence images (**e**) and quantifications of LipidTOX staining (**f**) and cytosolic BODIPY FL C16 signal (**g**) of treated HUVECs ($n = 10$ fields from 3 independent experiments). Scale bar, 5 μm. **h**–**j** LC-MS analysis showing the fractional abundance of $^{13}C_{16}$-labeled PA in the cytosol (**h**), $^{13}C_{16}$-labeled triglycerides in whole cells (**i**), and $^{13}C_{16}$-labeled PA in the culture medium (**j**) of HUVECs with the following treatment: OA (200 μM) for 12 h; DGAT1 overexpression for 48 h; or Atglistatin (10 μM) for 24 h ($n = 3$ samples). HUVECs were pretreated with $^{13}C_{16}$-PA (200 μM) for 24 h and rinsed with fresh medium before the above treatments. **k**–**p** Immunofluorescence images (**k**, **n**) and quantifications of LipidTOX staining (**l**, **o**) and ciliation (**m**, **p**) of HAECs treated with 200 μM OA and/or 200 μM SA or PA for 12 h ($n = 20$ fields from 3 independent experiments). Cells were treated with BSA or OA for 12 h, exposed to SA or PA for 12 h, and then serum-starved for 48 h. Scale bars, 20 μm. Data are presented as mean ± SEM. Statistical significance was determined by unpaired two-tailed Student's *t*-test (**b**, **c**, **h**, **j**), one-way (**d**), or two-way (**f**, **g**, **l**, **m**, **o**, and **p**) ANOVA with post hoc analysis. Source data are provided as a Source Data file.

To further explore the molecular mechanisms underlying LD accumulation-triggered ciliary loss, gas chromatography coupled to mass spectrometry (GC-MS) was performed to analyze the profiles of free fatty acids in OA-treated HUVECs. The results showed that OA-loaded HUVECs had remarkably reduced stearic acid (SA, 18:0) and PA (16:0) levels in the cytosol (Fig. 3b). In addition, elevating LD accumulation, either by promoting triglyceride synthesis via DGAT1 (dominant DGAT form in VECs) overexpression or by blocking lipolysis with Atglistatin treatment, exerted a similar effect on cytosolic fatty acid profiles (Supplementary Fig. 3b, c). Moreover, inhibition of triglyceride synthesis with a DGAT1 inhibitor, A922500, restored the reduction of cytosolic PA induced by the OA treatment (Fig. 3c). These results suggest that LD accumulation reduces cytosolic PA by sequestering it in triglycerides. In addition, it was observed that the concentration of total free fatty acids remained largely stable across all treated cells (Fig. 3d), suggesting the presence of a homeostatic mechanism for the stability of the overall free fatty acid level in endothelial cells. Together, these findings demonstrate that the accumulation of LDs in endothelial cells preferentially promotes the esterification of PA into triglycerides.

To further consolidate these findings, the distribution of PA in HUVECs was determined using a fluorescently labeled palmitate molecule, BODIPY-conjugated palmitate (BODIPY FL C16). Briefly, HUVECs were incubated with or without OA in the presence of BODIPY FL C16 for 12 h, followed by fluorescence confocal microscopy visualization of BODIPY FL C16. The results showed that in response to OA treatment, the free form cytosolic PA was substantially sequestered into LDs (Fig. 3e–g). Furthermore, we observed a time-dependent reduction in the abundance of free PA following OA treatment (Supplementary Fig. 3d–f). To confirm that PA was sequestered into LDs, LiveDrop was used to label nascent LDs[36]. Co-localization analysis showed that LiveDrop was distributed around BODIPY FL C16 (Supplementary Fig. 3g), indicating that PA was utilized for glyceride synthesis and LD formation. Next, DGAT activity in HUVECs was inhibited by co-treatment with A922500 and PF-06424439. DGAT inhibition effectively prevented OA-induced decrease in the concentration of cytosolic PA (Fig. 3e–g), demonstrating that DGAT-dependent sequestration of PA into LDs is responsible for the reduced PA abundance in the cytosol.

To provide additional evidence, a $^{13}C_{16}$-labeled PA tracing study was conducted. In brief, HUVECs were pretreated with $^{13}C_{16}$-labeled PA, rinsed with fresh medium, and exposed to OA, DGAT1 overexpression, or Atglistatin. Subsequently, a conventional liquid chromatography coupled with mass spectrometry (LC-MS) analysis was performed to determine the fractional abundance of $^{13}C_{16}$-labeled PA in both the cytosol and the culture medium. Additionally, a modified LC-MS analysis was employed to determine the fractional abundance of $^{13}C_{16}$-labeled triglycerides in whole-cell lysates and LDs isolated from treated cells. Consistent with our previous findings, the accumulation of LDs in HUVECs induced by OA, DGAT1 overexpression, or Atglistatin led to a dramatic decrease in the fractional abundance of $^{13}C_{16}$-labeled PA in the cytosol and an overall increase in $^{13}C_{16}$-labeled triglycerides in whole-cell lysates (Fig. 3h, i). Moreover, a notable presence of $^{13}C_{16}$-labeled triglycerides (>20% in many cases) was observed in LD samples (Supplementary Table 1), indicating a significant channeling of PA into triglycerides. The fractional abundance of $^{13}C_{16}$-labeled PA in the culture medium was determined by LC-MS to evaluate the efflux of fatty acids by endothelial cells. No significant impact was observed in the OA-treated group. However, DGAT1 overexpression resulted in a slight decrease, while Atglistatin treatment caused a slight increase in the fractional abundance of $^{13}C_{16}$-labeled PA in the culture medium (Fig. 3j). While OA treatment, DGAT1 overexpression, and Atglistatin treatment can all stimulate LD accumulation, they may have distinct impacts on the dynamics/turnover of LDs, which could potentially lead to a variation in the efflux of fatty acids by endothelial cells. Collectively, the above results provide compelling evidence that LD accumulation reduces cytosolic PA availability by promoting its esterification into triglycerides.

To determine whether ciliation responds to changes in SA or PA levels, ciliogenesis was induced in HAECs in the presence of SA or PA. Immunofluorescence microscopy showed that PA, but not SA, was able to restore OA-induced ciliary defects (Fig. 3k–p). Similar results were also observed in HUVECs (Supplementary Fig. 4a–f). A previous study showed that PA treatment led to a reduction in the percentage of ciliated hypothalamic neurons, whereas the number of cilia in hypothalamic astrocytes remained unaffected[37]. Using the same method described in this study, we examined the effects of α-linolenic acid (ALA) and PA on the ciliation of HAECs. Immunofluorescence microscopy showed that PA, but not ALA, effectively restored OA-induced ciliary defects (Supplementary Fig. 4g–i). Consistent with these results, blocking LD lipolysis with Atglistatin treatment disrupted ciliary homeostasis in HUVECs, and this was also reversed by exogenous PA supplementation (Supplementary Fig. 4j–l). To further confirm the effect of PA on ciliary homeostasis, HUVECs were treated with C75, a fatty acid synthase (FASN) inhibitor, to suppress endogenous PA synthesis. Immunostaining showed that FASN inhibition resulted in fewer cilia, and this was effectively rescued by exogenous PA supplementation (Supplementary Fig. 4m–o). These findings strongly indicate that PA availability is essential for endothelial ciliation.

Reduced PA availability decreases ciliary protein S-palmitoylation and stability

In addition to serving as a source of energy, PA can modulate the function of numerous proteins at the post-translational level by mediating protein S-palmitoylation through the formation of thioester bonds[38]. Numerous ciliary proteins require S-palmitoylation modification for proper transport and localization[39]. To determine whether protein S-palmitoylation is involved in LD-associated ciliary loss, HUVECs were treated with chemical inhibitors of palmitoylation (2-bromopalmitate; 2-BP) and depalmitoylation (Palmostatin B; PB). Immunofluorescence imaging revealed that inhibition of S-palmitoylation significantly suppressed ciliation, whereas enhancement of protein S-palmitoylation largely restored OA-induced ciliary loss (Fig. 4a, b). Consistently, exogenous PA supplementation significantly rescued ciliary loss in 2-BP-treated HAECs (Fig. 4c, d) and HUVECs (Supplementary Fig. 6a–c). These results thus indicate that a decrease in protein S-palmitoylation is responsible for LD-associated ciliary loss.

To identify protein S-palmitoylation substrates involved in LD-associated ciliary loss, S-palmitoylated proteins in HUVECs cultured with or without OA were analyzed using an acyl-biotin exchange (ABE) assay combined with mass spectrometry (MS) (Supplementary Fig. 5a). KEGG Pathway analysis and Cluster of Orthologous Groups of proteins (COG) annotation analysis of differentially palmitoylated proteins revealed that OA treatment upregulated palmitoylated proteins predominantly involved in metabolic pathways and downregulated the palmitoylation of various cytoskeletal proteins (Fig. 4e, f and Supplementary Fig. 5b). To further explore the molecular mechanism underlying the OA-induced ciliary loss, a total of 33 cilia-related proteins were identified from the list of palmitoylated proteins. Among them, 18 proteins can localize to the plasma membrane (Fig. 4g, h and Supplementary Table 2). Given that palmitoyl-proteome screening could yield false-positive results, we used a protein-specific ABE assay to verify the S-acylation of specific candidate proteins, such as pericentriolar material 1 (PCM1), kinesin family member 3 A (KIF3A), centrosomal protein 131 (CEP131), small GTPase RAB8A, and ADP ribosylation factor like GTPase 13B (ARL13B), in cultured primary mouse aortic endothelial cells (MAECs). The results showed that OA treatment significantly decreased the S-palmitoylation level of ARL13B, RAB8A, and CEP131, with the most dramatic reduction observed in

https://doi.org/10.1038/s41467-024-52621-x

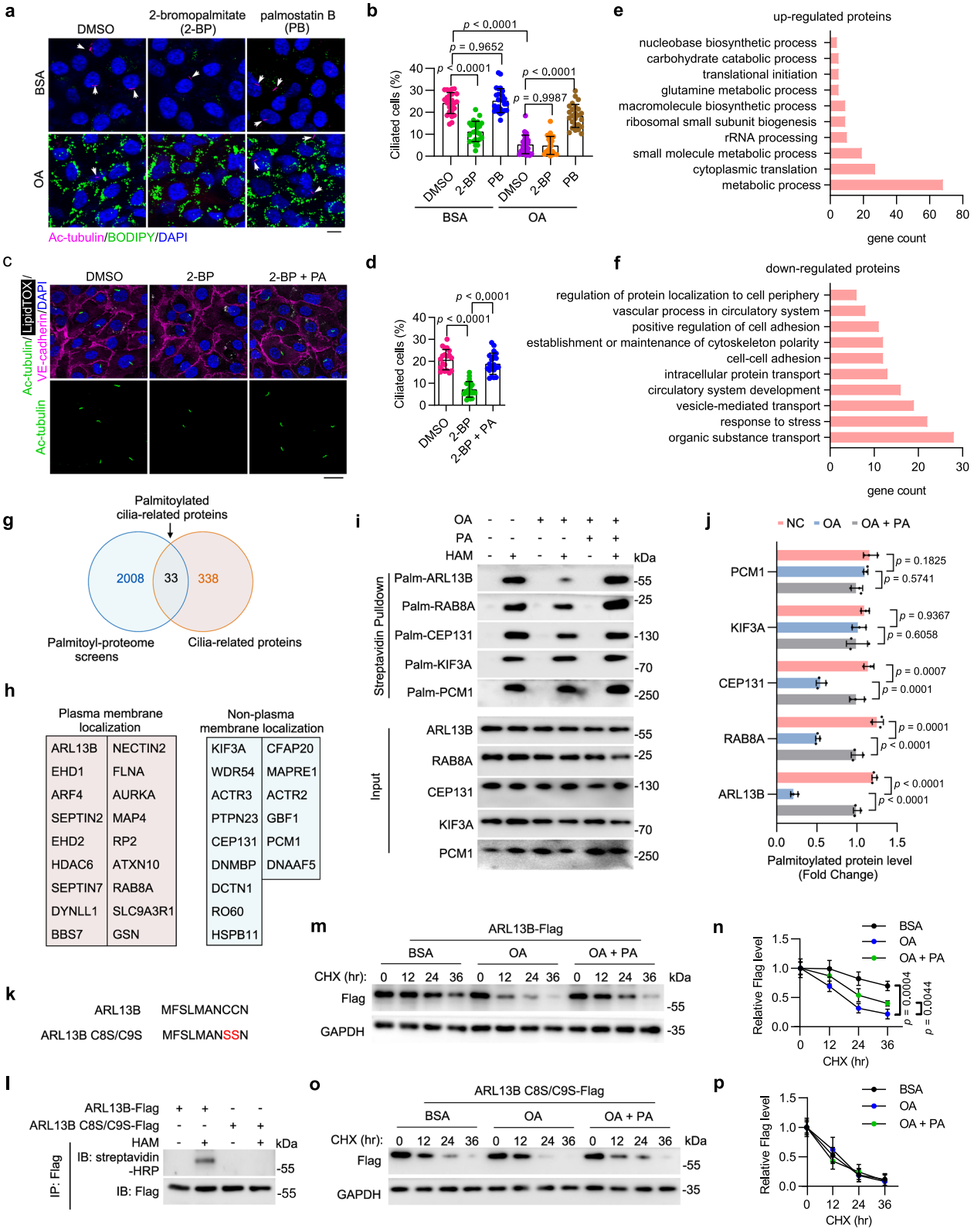

ARL13B S-palmitoylation. Moreover, PA supplementation effectively restored S-palmitoylation of all three proteins (Fig. 4i, j).

ARL13B, a member of the ARF family of regulatory GTPases, is essential for cilia architecture, protein transport and cilium-dependent signaling[40–42]. To further evaluate the role of PA in maintaining ciliary homeostasis, MAECs were treated with 2-BP and subsequently supplemented with exogenous PA. The IP-ABE assay showed that PA supplementation largely abolished the inhibition of ARL13B S-palmitoylation induced by 2-BP treatment (Supplementary Fig. 6d, e). In addition, FASN inhibition by C75 effectively suppressed ARL13B S-palmitoylation in MAECs, which was also restored by exogenous PA supplementation (Supplementary Fig. 6f, g). Protein S-palmitoylation has been shown to be involved in the regulation of protein stability. Indeed, a cycloheximide (CHX) pulse-chase assay

Fig. 4 | Reduced PA availability decreases ciliary protein S-palmitoylation and stability. a, **b** Immunofluorescence images (**a**) and quantification of ciliation (**b**, $n = 20$ fields from 3 independent experiments) of HUVECs treated with DMSO, 2-Bromopalmitate (2-BP, 50 μM), or Palmostatin B (PB, 10 μM) for 24 h, exposed to BSA or oleic acid (OA, 200 μM) for 12 h, and then serum-starved for 48 h. Scale bar, 10 μm. **c**, **d** Immunofluorescence images (**c**) and quantification of ciliation (**d**, $n = 20$ fields from 3 independent experiments) of treated HAECs. Scale bar, 20 μm. **e**, **f** COG analysis of upregulated (**e**) or downregulated (**f**) S-palmitoylated proteins upon OA treatment in HUVECs. **g** Venn diagram showing the overlap of S-palmitoylated proteins (identified in our study) and cilia-related proteins (based on the GO database). **h** Annotation of subcellular localization of palmitoylated cilia-related proteins identified in (**g**) (based on the Human Protein Atlas database). **i**, **j** Detection (**i**) and quantification (**j**) of S-palmitoylation levels of indicated cilia-related proteins ($n = 3$ samples). MAECs were pre-incubated with OA (200 μM) or BSA for 12 h and then supplemented with PA (200 μM) for another 12 h. In hydroxylamine+ (HAM+) groups, the palmitate residues were cleaved off and replaced with biotin, which allows the detection of palmitoylated proteins by IP-ABE. **k**, **l** HUVECs were overexpressed with ARL13B-Flag or ARL13B C8S/C9S-Flag (**l**), and the S-palmitoylation level of ARL13B-Flag and ARL13B C8S/C9S-Flag was examined by IP-ABE and immunoblotting. **m**–**p** HUVECs were overexpressed with ARL13B-Flag or ARL13B C8S/C9S-Flag, pretreated with BSA, OA (200 μM), or OA+PA (200 μM, respectively) for 12 h and then treated with CHX (20 μg/mL) for the indicated time. The levels of ARL13B-Flag and ARL13B C8S/C9S-Flag were examined by immunoblotting (**m**, **o**) and quantified by densitometry (**n**, **p**) ($n = 3$ samples). Data are presented as mean ± SEM. Statistical significance was determined by one-way (**d**, **j**, **n**, and **p**) or two-way (**b**) ANOVA with post hoc analysis. Source data are provided as a Source Data file.

showed that treatment of HUVECs with 2-BP significantly accelerated ARL13B degradation (Supplementary Fig. 6h, i). To further investigate the role of decreased PA availability mediated by OA on ARL13B stability, we generated an ARL13B mutant with dual mutations of cysteine 8 and cysteine 9 to serines (ARL13B C8S/C9S) as previously reported[43] and assessed the effect of C8S/C9S mutation on ARL13B S-palmitoylation through IP-ABE. The C8S/C9S mutation resulted in a drastic loss of ARL13B S-palmitoylation (Fig. 4k, l). OA treatment, similar to the 2-BP treatment, significantly reduced the half-life of ARL13B in HUVECs (Fig. 4m, n). Additionally, we found that exogenous PA supplementation had no effect on the degradation of the ARL13B C8S/C9S mutant but partially rescued the decrease in ARL13B stability induced by OA (Fig. 4m–p), suggesting that the OA-mediated reduction in PA availability decreases the half-life of ARL13B protein by suppressing its S-palmitoylation level. A previous study has shown that myristoylation sequence insertion significantly restored the ciliary localization but not the protein stability of ARL13B C8S/C9S[43]. We then overexpressed ARL13B-GFP or ARL13B-GFP Myr (myristoylation sequence-inserted) in MAECs supplemented with or without OA. Immunofluorescence analysis showed that ARL13B-GFP Myr, but not ARL13B-GFP, successfully restored the ciliation of OA-treated cells (Supplementary Fig. 6j–l). Notably, despite its prominent signal, exogenously expressed ARL13B-GFP showed no apparent ciliary localization in OA-treated cells (Supplementary Fig. 6j–l). Together, these results suggest that both the protein level and the ciliary localization of ARL13B are essential for proper endothelial ciliation.

S-palmitoylation is catalyzed by the zinc finger aspartate-histidine-histidine-cysteine (DHHC) domain-containing family of palmitoyl S-acyltransferases, while depalmitoylation is mediated by S-depalmitoylases, including acyl-protein thioesterases (APTs) and *α/β*-hydrolase domain-containing proteins[44,45]. Their expression levels were then determined by qRT-PCR. The results showed that in cultured HUVECs, OA treatment had no significant effect on the expression level of any palmitoylase or depalmitoylase (Supplementary Fig. 6m, n). Taken together, these findings indicate that PA availability is essential for the regulation of protein S-palmitoylation in the vascular endothelium.

SCD1 disrupts ciliary homeostasis by reducing PA availability

SCD1 catalyzes the desaturation of saturated fatty acids (mainly PA and SA) into monounsaturated fatty acids (Fig. 5a). Our qRT-PCR and Western blot analyses showed that the transcription and protein production of SCD1 were both significantly upregulated in VECs from HFD-fed mice (Fig. 5b–d). GC-MS analysis confirmed that SCD1 overexpression decreased PA (16:0) and SA (18:0) levels and increased palmitoleic acid (POA, 16:1) and OA (18:1) levels in HUVECs (Fig. 5e). We then sought to determine whether a change in the ratio of PA (16:0) to POA (16:1) could affect endothelial ciliation in HUVECs. Immunostaining results showed that fatty acid treatment with a lower PA/POA ratio dramatically stimulated LD generation and suppressed ciliation, while fatty acid treatment with a higher PA/POA ratio had no significant effects on LD formation and ciliation, as compared to untreated HUVECs (Fig. 5f–h). These results demonstrate that PA has a protective role in maintaining endothelial cilia during fatty acid overloading. In addition, a simple supplementation of PA effectively rescued the ciliary defect induced by SCD1 overexpression in HAECs (Fig. 5i–k).

To evaluate the involvement of SCD1 in endothelial ciliation, an IP-ABE assay was performed to determine the effect of SCD1 on ARL13B palmitoylation. The results showed that SCD1 overexpression induced a substantial reduction in ARL13B palmitoylation in HUVECs, which was effectively reversed by PA supplementation (Fig. 5l). The protein half-life assay showed that enforced SCD1 expression in HUVECs led to faster degradation of ARL13B, and exogenous PA supplementation partially rescued the SCD1-mediated reduction in ARL13B protein stability (Fig. 5m, n). These results suggest that HFD-induced SCD1 elevation in VECs may contribute to the progression of atherosclerosis by reducing cytosolic PA availability and disrupting endothelial ciliation.

SCD1 inhibition attenuates the progression of atherosclerosis in an endothelial cilia-dependent manner

Previously, it has been shown that SCD1 deficiency mediated by antisense oligonucleotides exhibits distinct roles in the $Ldlr^{-/-}Apob^{100/100}$ model of atherosclerosis and the model induced by chronic intermittent hypoxia[31,32]. Our results suggest that SCD1 activity in VECs reduces cytosolic PA availability and disrupts ciliation, which could contribute to the progression of atherosclerosis. To determine the involvement of SCD1 and endothelial cilia in atherosclerosis, we generated Tek-Cre + /$IFT88^{fl/fl}$/$ApoE^{KO}$ ($IFT88^{EC\ KO}$;$ApoE^{KO}$) mice, which carry an endothelial-specific deletion of *intraflagellar transport 88* (*Ift88*), a gene encoding an essential component for ciliogenesis and maintenance, on a hyperlipidemic $ApoE^{KO}$ background. The depletion of IFT88 in the knockout mice was confirmed at both genomic and protein levels (Supplementary Fig. 7a, b).

$IFT88^{EC\ KO}$;$ApoE^{KO}$ and $IFT88^{fl/fl}$;$ApoE^{KO}$ ($ApoE^{KO}$) mice were fed with a HFD for 6 weeks to induce atherosclerotic lesions and were then maintained on the HFD for an additional 6 weeks, during which SCD1 inhibitor (A939572) or vehicle control was administered intravenously every other day. Analysis of serum lipid composition showed that except for a slight decrease in the level of serum triglycerides, A939572 treatment induced no significant changes in the serum levels of high-density lipoprotein cholesterol (HDL-C), low-density lipoprotein cholesterol (LDL-C), and total cholesterol (CHO) in $ApoE^{KO}$ and $IFT88^{EC\ KO}$;$ApoE^{KO}$ mice (Supplementary Fig. 7c–f). These results are consistent with previous reports indicating that endothelial cilia do not exert an influence on circulating lipid levels in the context of atherosclerosis[8]. LD synthesis and ciliation in VECs of the aortic arch were characterized by *en face* immunostaining. The result showed that SCD1 inhibition significantly diminished LD formation, while deletion of *Ift88* essentially ablated endothelial cilia in

https://doi.org/10.1038/s41467-024-52621-x

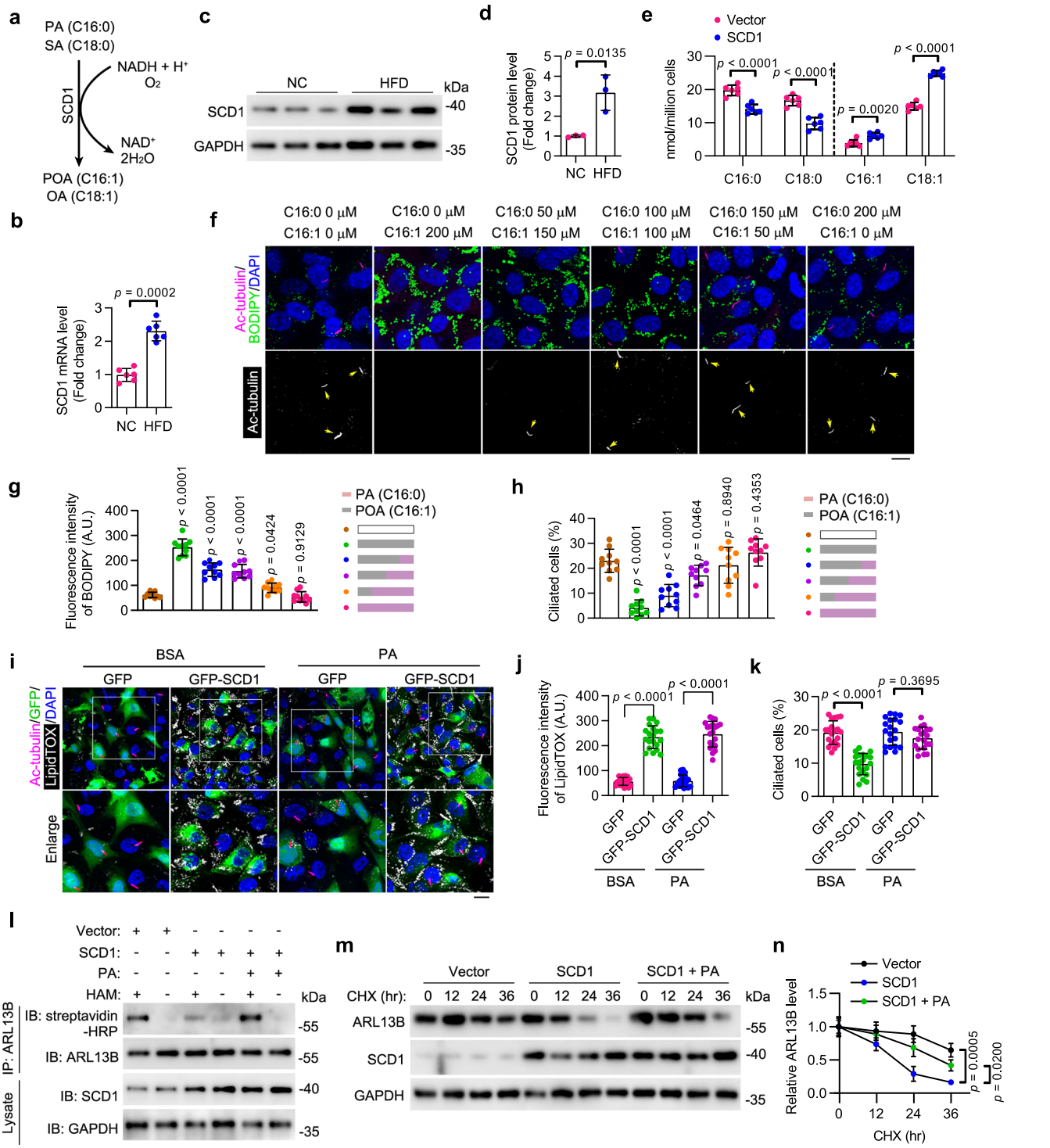

Fig. 5 | HFD-stimulated SCD1 disrupts ciliary homeostasis by reducing PA availability. a Schematic of the reaction catalyzed by SCD1. **b** The mRNA level of SCD1 in MAECs isolated from ApoE^{KO} mice fed NC or HFD ($n = 6$ mice). **c**, **d** Immunoblotting (**c**) and quantification (**d**, $n = 3$ mice) of the protein level of SCD1 in MAECs isolated from ApoE^{KO} mice fed NC or HFD. **e** Levels of indicated fatty acids in HUVECs with or without SCD1 overexpression ($n = 6$ samples). **f**–**h** Immunofluorescence images (**f**) and quantifications of BODIPY staining (**g**) and ciliation (**h**) of HUVECs treated with palmitic acid (PA) and palmitoleic acid (POA) at the indicated concentration for 12 h, followed by serum starvation for 48 h ($n = 10$ fields from 3 independent experiments). Scale bar, 10 μm. **i**–**k** Immunofluorescence images (**i**) and quantifications of LipidTOX staining (**j**) and ciliation (**k**) of BSA- or PA (200 μM)-treated HAECs with or without SCD1 overexpression ($n = 20$ fields from 3 independent experiments). Boxed areas are enlarged in the bottom panel. Scale bar (for enlarged images), 10 μm. **l** HUVECs with or without SCD1 overexpression were treated with BSA or PA (200 μM) for 12 h. IP-ABE and immunoblotting were performed to determine the level of ARL13B S-palmitoylation. pcDNA3.1 vector was used as the Vector control. **m**, **n** HUVECs with or without SCD1 overexpression were treated with or without PA (200 μM) for 12 h. 20 mg/mL cycloheximide (CHX) was then added for the indicated time. The levels of ARL13B and SCD1 were examined by immunoblotting (**m**) and quantified by densitometry (**n**) ($n = 3$ samples). Data are presented as mean ± SEM. Statistical significance was determined by unpaired two-tailed Student's *t*-test (**b**, **d**, and **e**), one-way (**g**, **h**, **n**), or two-way (**j**, **k**) ANOVA with post hoc analysis. Source data are provided as a Source Data file.

https://doi.org/10.1038/s41467-024-52621-x

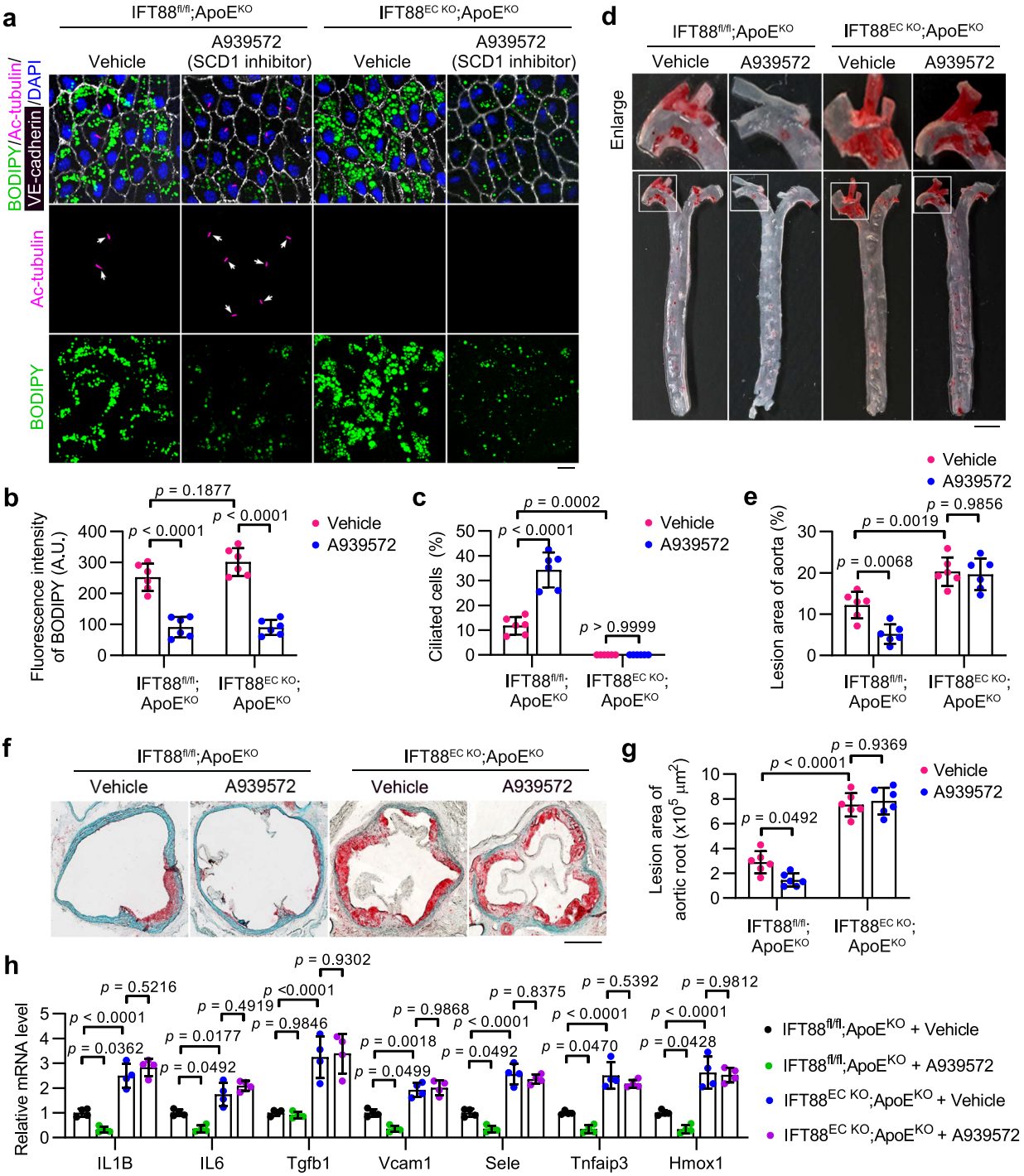

Fig. 6 | SCD1 inhibition attenuates atherosclerosis progression in an endothelial cilia-dependent manner. a–c *En face* immunofluorescence images (**a**) and quantifications of BODIPY staining (**b**) and ciliation (**c**) of aortic arch VECs from IFT88$^{EC\,KO}$;ApoE^{KO} and littermate ApoE^{KO} mice intravenously injected with the SCD1 inhibitor A939572 (5 mg/kg body weight/2 days) or vehicle for 4 weeks after an 8-week HFD feeding ($n = 6$ mice). Scale bar, 10 μm. **d** Representative images of Oil Red O (ORO) staining of atherosclerosis lesions on the aorta of IFT88$^{EC\,KO}$;ApoE^{KO} and littermate ApoE^{KO} mice treated as described in (**a**). Boxed areas are enlarged in the top panel. Scale bar (for enlarged images), 1 mm. **e** Quantification of atherosclerotic lesions shown in (**d**) ($n = 6$ mice). **f** Representative ORO staining in the aortic root of IFT88$^{EC\,KO}$;ApoE^{KO} and littermate ApoE^{KO} mice treated as described in (**a**). Scale bar, 500 μm. **g** Quantification of atherosclerotic lesions shown in (**f**) ($n = 6$ mice). **h** Transcriptional levels of *IL1B*, *IL6*, *Tgfb1*, *Vcam1*, *Sele*, *Tnfaip3*, and *Hmox1*, in mice treated as described in (**a**) ($n = 4$ mice). Data are presented as mean ± SEM. Statistical significance was determined by two-way ANOVA with post hoc analysis. Source data are provided as a Source Data file.

VECs of both ApoE^{KO} and IFT88$^{EC\,KO}$;ApoE^{KO} mice. Strikingly, SCD1 inhibition greatly promoted endothelial ciliation in ApoE^{KO} mice (Fig. 6a–c and Supplementary Fig. 7g–i).

ORO staining showed that inhibition of SCD1 by A939572 treatment significantly diminished atherosclerotic lesion formation in ApoE^{KO} mice (Fig. 6d–g). However, the protective effect of SCD1 inhibition was completely ablated by *Ift88* knockout-mediated endothelial ciliary loss (Fig. 6d–g). Additionally, we detected decreased transcriptional levels of numerous inflammatory factors in the aortic arch of ApoE^{KO} mice after A939572 treatment, including genes encoding the

https://doi.org/10.1038/s41467-024-52621-x

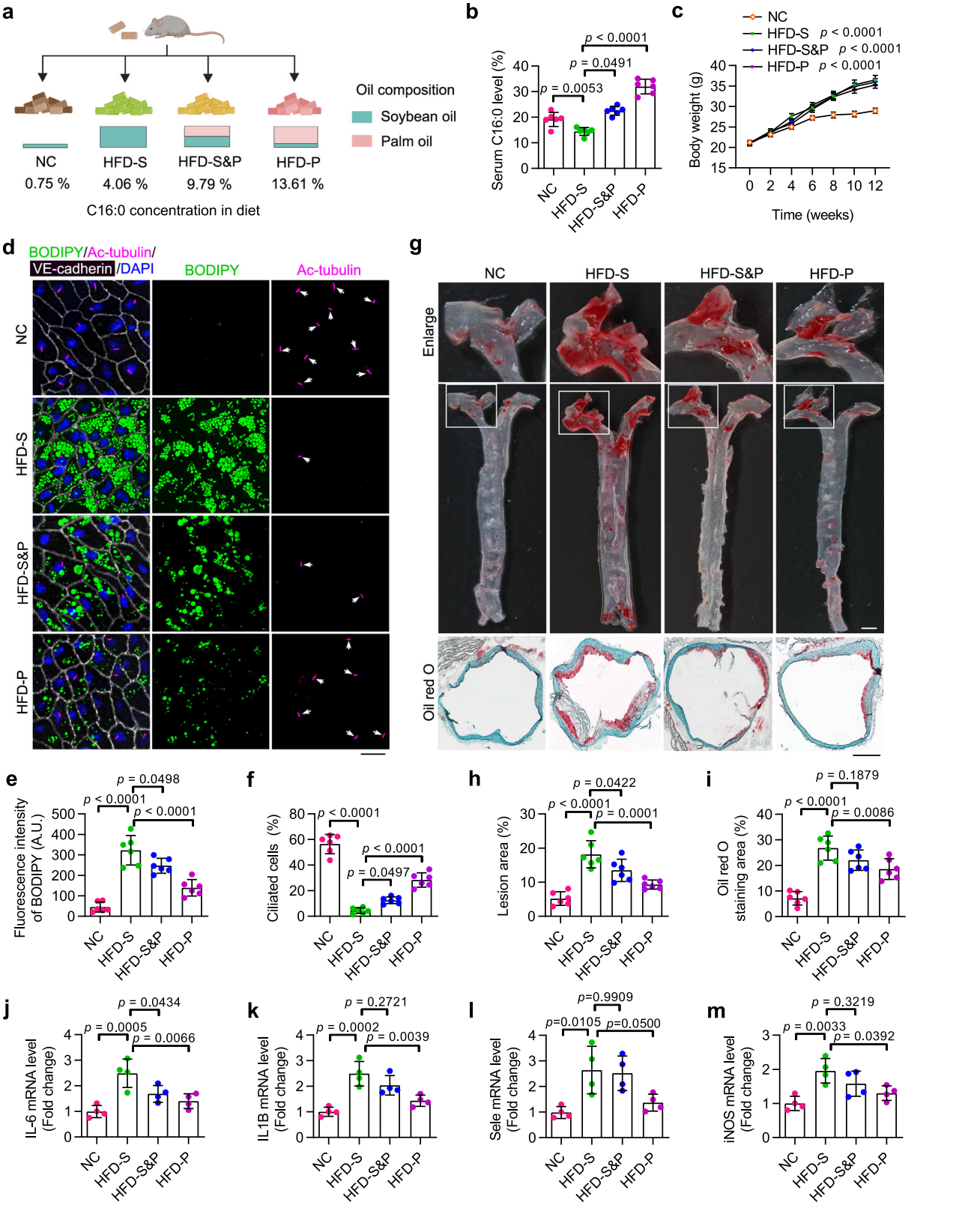

proinflammatory cytokines interleukin 1 beta (*IL1B*), interleukin 6 (*IL6*), transforming growth factor beta 1 (*Tgfb1*), the inflammatory adhesion molecules *Vcam1* and E-selectin (*Sele*), the NF-κB target TNF alpha-induced protein 3 (*Tnfaip3*), as well as the stress responder heme oxygenase 1 (*Hmox1*), and these effects were also ablated by endothelial *Ift88* knockout (Fig. 6h), which is consistent with previous findings[8]. Altogether, our data show that the SCD1 inhibitor A939572, when administrated intravenously, mitigates atherosclerosis in an endothelial cilia-dependent manner.

It has been demonstrated that the exogenous addition of high levels of PA induces ER stress in cells[21]. MAECs were then exposed to PA at various concentrations, and the ER stress level was determined by Western blot analysis of protein kinase RNA-like endoplasmic reticulum kinase (PERK) phosphorylation and C/EBP-homologous protein

Fig. 7 | A PA-enriched diet preserves VEC cilia and alleviates the progression of atherosclerosis. a Eight-week-old ApoE^{KO} mice were divided into four groups and fed indicated diets for 12 weeks. NC normal chow, HFD high-fat diet, S soybean oil, P palm oil. **b**, **c** Serum palmitic acid (PA) level (**b**) and body weight (**c**) of ApoE^{KO} mice treated as described in (**a**) ($n = 6$ mice). **d**–**f** *En face* immunofluorescence images (**d**) and quantifications of BODIPY staining (**e**) and ciliation (**f**) of VECs of the aortic arch from ApoE^{KO} mice treated as described in (**a**) ($n = 6$ mice). Scale bar, 20 μm. **g** Oil Red O (ORO) staining showing atherosclerotic lesions in the aortic tree and the aortic root obtained from mice treated as described in (**a**). Boxed areas are enlarged in the top panel. Scale bar (for the middle panel), 2 mm; Scale bar (for the bottom panel), 400 μm. **h**, **i** Quantification of atherosclerotic lesions in the aortic tree (**h**) and the aortic root (**i**) shown in (**g**) ($n = 6$ mice). **j**–**m** Transcriptional levels of *IL6*, *IL1B*, *Sele*, and *iNOS* in the aorta of ApoE^{KO} mice treated as described in (**a**) ($n = 4$ mice). Data are presented as mean ± SEM. Statistical significance was determined by one-way ANOVA with post hoc analysis. Panel (**a**) was created with BioRender.com and released under a Creative Commons Attribution-NonCommercial-NoDerivs 4.0 International license. Source data are provided as a Source Data file.

(CHOP) expression. A mild ER stress was observed only at the highest concentration of PA (200 μM) (Supplementary Fig. 7j, k). In addition, Western blot analysis of aortic arch samples revealed that the administration of the SCD1 inhibitor, A939572, to mice, did not stimulate ER stress (Supplementary Fig. 7l, m). It has been shown that the primary cilium plays a crucial role in activating autophagy and preventing senescence in endothelial cells[46]. In addition, PA can induce endothelial autophagy and senescence in HUVECs[47,48]. We then investigated the effects of PA and OA on autophagy and senescence in HAECs by examining the levels of LC3 lipidation and the expression of the senescence marker p16. The results revealed that PA enhanced both autophagy and senescence, whereas OA suppressed autophagy but had no significant effect on senescence (Supplementary Fig. 7n, o). These findings were further corroborated by the staining of LC3 puncta and senescence-associated β-galactosidase (SA-β-gal) (Supplementary Fig. 7p–r). Increased ER stress and senescence are considered detrimental to endothelial health, while enhanced autophagy is considered beneficial. Therefore, the effect of PA on vascular endothelium could vary depending on specific conditions, as exposure to PA may have both negative and positive effects on endothelial function through various mechanisms.

A PA-enriched diet preserves VEC cilia and alleviates atherosclerosis progression

PA can be synthesized through de novo lipogenesis or directly obtained from dietary fats. Given the potential protective effects of PA shown in maintaining endothelial ciliary homeostasis and restricting atherosclerosis progression, we next asked whether a PA-enriched diet could mitigate the development of atherosclerosis. To answer this, ApoE^{KO} mice were exposed to a series of different diets containing various amounts of PA for 12 weeks (Supplementary Table 3 and Fig. 7a). A GC-MS analysis was conducted to examine the fatty acid levels in the serum of mice subjected to different diets (Fig. 7b and Supplementary Fig. 8a–c). The results revealed that mice fed a low PA (4.06%) soybean oil-based HFD (HFD-S) had significantly decreased serum PA level, as compared to NC-fed mice. Meanwhile, a high PA (13.61%) palm oil-based HFD (HFD-P) induced a dramatic increase in the serum PA level (~1.5 folds of NC-fed group; ~2 folds of HFD-S-fed group) (Fig. 7b). Notably, the three different types of HFD stimulated comparable increases in body weight (Fig. 7c), suggesting that any potential role of PA in atherosclerosis is independent to body weight.

En face immunostaining showed that compared to the NC-fed group, mice fed with a low PA soybean oil-based HFD exhibited substantially enhanced LD accumulation and significantly disrupted ciliation in VECs. In contrast, mice fed a high PA palm oil-based HFD displayed significantly fewer LDs and enhanced endothelial ciliation, as compared to the mice fed a low PA soybean oil-based HFD (Fig. 7d–f and Supplementary Fig. 8d–f). To determine the effect of various diets on the progression of atherosclerosis, aortic samples were stained with ORO to examine the atherosclerotic lesion area. The results revealed that among the three types of HFD, the atherosclerotic plaque burden in both the entire aorta and the root area was significantly milder in mice fed with a high PA palm oil-based HFD (Fig. 7g–i). In addition, qRT-PCR analysis of the whole aorta showed that transcriptional levels of several inflammatory factors, including IL6, IL1B, Sele and iNOS, were significantly lower in mice fed a high PA palm oil-based HFD (Fig. 7j–m). These results thus indicate that even in the presence of a HFD, a simple dietary supplementation of PA could effectively alleviate the progression of atherosclerosis. Collectively, our findings demonstrate the potential of a feasible dietary intervention strategy for the prevention and treatment of atherosclerosis.

Discussion

Atherosclerosis, the leading cause of coronary artery disease[49], is initiated and progressed by vascular endothelial dysfunction[50]. Recent studies have highlighted the protective role of cilia in endothelial function against the development of atherosclerosis[8]. In the present study, we observed concurrent LD accumulation and ciliary loss in VECs during atherosclerosis progression. LD accumulation reduces cytosolic PA availability and suppresses the S-palmitoylation of ciliary proteins, leading to impaired ciliation in VECs and contributing to the development of atherosclerosis. Moreover, we show that restoring PA availability mitigates the atherogenic effects of disrupted ciliary homeostasis. These findings thus demonstrate that the accumulation of LDs in VECs exacerbates the progression of atherosclerosis in an endothelial cilia-dependent manner.

The present study provides strong evidence for the involvement of primary cilia in endothelial LD-mediated atherosclerosis exacerbation. However, it is still possible for LDs to exacerbate atherosclerosis via cilium-independent mechanisms. In line with this argument, two very recent studies linked endothelial LD accumulation to the pathogenesis of atherosclerosis[51,52]. Both studies employed VE-cadherin-Cre-driven endothelium-specific ATGL knockout mice and demonstrated that eNOS mRNA destabilization and ER stress-induced inflammation contribute to the acceleration of atherosclerosis. Our current work, which utilizes comprehensive in vitro and in vivo models, further demonstrates that cytosolic PA availability and primary cilia in endothelial cells play crucial roles in the exacerbation of atherosclerosis mediated by endothelial LDs. Therefore, we believe our work to be a significant scientific advance that, when combined with the two most recent discoveries, offers a comprehensive picture of the function of LDs in vascular health.

In our current study, IFT88$^{EC\,KO}$ mice were utilized to demonstrate that reduced endothelial ciliation is an important mechanism underlying the exacerbation of atherosclerosis mediated by endothelial LDs. Regarding the dynamics and functions of primary cilia in vascular health, seemingly contradictory observations have been documented[8,53,54]. A potential explanation is that the induction of primary cilia in certain models of atherosclerosis may represent the activation of a protective mechanism. Additionally, specific environmental factors, such as the patterns of blood flow in the aorta, may fine-tune endothelial ciliation in a context-dependent manner. Therefore, further investigation is warranted to explore the upstream mechanisms controlling the assembly and dynamics of endothelial cilia in specific regions of the aorta, as well as their distinct pathophysiological functions in vascular health. Another subject worth pursuing is whether blocking the disassembly of endothelial cilia, either in the whole body or specifically in the aortic arch, could provide a preventive effect against atherosclerosis.

In the arterial tree, primary cilia are enriched in regions experiencing disturbed shear stress, such as branches, bifurcations, and inward curves[55]. In this study, we found a significant accumulation of LD in VECs from mice fed a HFD, leading to disrupted ciliary homeostasis. Previous study has demonstrated that preadipocytes gradually lose their cilia during maturation, which coincides with LD formation[56]. This LD-cilium non-compatibility has also been observed in other cell types, including brown adipocytes and hepatocytes[57,58]. Whether a change in the cytosolic PA availability and a subsequent reduction in the S-palmitoylation of ciliary proteins underlies the LD-associated ciliary loss in these cells may be worth further investigation.

We identified a PA-mediated contact-independent mechanism for the LD-cilium interaction. However, our research was unable to rule out the possibility that extremely small LDs may reside adjacent to the basal body or even within cilia. This question should be able to be answered by a more in-depth analysis, preferably using electron microscopy. It's also worth noting that various vertebrate species, including fish and mammals, have LDs that contain carotenoid pigments and neutral lipids in the inner segment of their cone photoreceptors. These LDs are interposed in the light pathway through the photoreceptor and alter the intensity and spectrum of light reaching the photosensitive outer segment[59]. Whether and how these LDs interact directly with the connecting cilia in photoreceptors warrants further study.

Protein acylation, which involves the covalent addition of diverse types of acyl groups to proteins, is essential for multiple physiological and pathological cellular processes. N-acylation, S-acylation, and O-acylation are the most prevalent forms of protein acylation. A previous study revealed that PA-mediated S-palmitoylation constitutes 74% of all S-acylated proteins in platelets, making it the most prevalent form of protein S-acylation[60]. POA participates in O-palmitoleoylation, a relatively rare form of protein acylation. Despite its rarity, studies have demonstrated that O-palmitoleoylation of Wnt proteins is critical for the proper functioning of Wnt signaling[61,62]. In our study, we mainly focused on PA-mediated S-palmitoylation and demonstrated that S-palmitoylation of ciliary proteins, including ARL13B, promotes endothelial ciliation. POA, similar to monounsaturated OA, exhibits an enhanced capability to induce the formation of LDs. The potential role of POA-mediated O-palmitoleoylation in endothelial ciliation and atherosclerosis was not determined. In addition, previous studies have indeed shown that RAB8A and CEP131 play important roles in ciliogenesis and that RAB8A could undergo palmitoylation[63–65]. Further investigation of the existence and function of S-palmitoylation of RAB8A and CEP131 in the context of endothelial ciliation and atherosclerosis could lead to important new findings.

As a key enzyme in fatty acid metabolism, SCD1 catalyzes the formation of monounsaturated oleate and palmitoleate. Dysregulation of SCD1 activity has been associated with cancer, obesity, metabolic syndrome, and atherosclerosis[31,66–69]. There have been contradictory reports regarding the contribution of SCD1 to the progression of atherosclerosis[70,71]. Our results suggest that diet-induced SCD1 elevation acts in synergy with LD formation to restrict cytosolic PA availability and VEC ciliation. To assess the role of SCD1 activity in VECs in atherosclerosis, the SCD1 inhibitor A939572 was administrated intravenously to $ApoE^{KO}$ mice. The results showed that this SCD1 inhibition approach effectively attenuated HFD-induced atherosclerosis. Consistent with this finding, a previous study reported that SCD1 deficiency attenuates chronic intermittent hypoxia-induced dyslipidemia and atherosclerosis in mice[31]. On the other hand, studies have also shown that SCD1 inhibition promotes atherosclerosis in the $Ldlr^{KO}Apob^{100/100}$ mouse model of hyperlipidemia and atherosclerosis[32,69]. We speculate that the model-specific HDL cholesterol level might contribute to the discrepancy between the above findings. In the $Ldlr^{KO}Apob^{100/100}$ mouse model, SCD1 deficiency was accompanied by a ~50% reduction in the HDL-C level, which could contribute to increased atherosclerosis. In contrast, in the chronic intermittent hypoxia mouse model, antisense oligonucleotide-mediated SCD1 deficiency resulted in a ~20% increase in the HDL-C level. In our study, SCD1 inhibition by intravenous administration of A939572 showed no obvious effect on the serum HDL-C level in $ApoE^{KO}$ mice. Therefore, we propose that inhibiting SCD1 activity, specifically in VECs, may represent an opportunity to combat atherosclerosis.

SCD1 is widely expressed across various tissues, including the adipose tissue, liver, and heart. Therefore, the particular approaches utilized for manipulating SCD1 could substantially influence the final outcome. A recent study reported that loss of endothelial SCD1 increased vascular inflammation[72]. As a critical signaling hub for lipid metabolism, SCD1 plays an essential role in maintaining metabolic and tissue homeostasis. Hence, a complete lack of endothelium SCD1 may result in elevated vascular damage through various mechanisms. In previous studies, the SCD1 inhibitor A939572 was administered to mice orally every one or two days with a dose ranging from 10 to 100 mg/kg body weight[73–75]. We utilized a modified methodology in which the mice received tail vein injections of A939572 (5 mg/kg body weight) every other day, which could allow direct exposure of the vascular endothelium to the SCD1 inhibitor. While there are numerous beneficial effects associated with inhibiting SCD1 to combat diseases like atherosclerosis, it's crucial to acknowledge that SCD1 activity in specific tissues, such as the skin, may serve a protective function in metabolism[31,69]. It's worth noting that the mouse line, the diets used to induce atherosclerosis, and the approaches used to inhibit SCD1 inhibition varied among studies. Although the progression of atherosclerosis in humans cannot be accurately simulated by any mouse model of atherosclerosis, future research that employs a "standardized" animal model of atherosclerosis could help resolve this issue. Therefore, future translational studies involving SCD1 should be carefully evaluated to formulate an optimized therapeutic regimen.

Edible oils rich in saturated fatty acids, such as palm oil, have been widely believed to be detrimental to the cardiovascular system, yet a growing number of studies have demonstrated that a palm oil-rich diet could have beneficial effects on human health[76–78]. Studies comparing the health effects induced by diets enriched with various types of oil showed that palm oil-rich diets improved serum lipid profiles, compared to trans fatty acid-rich diets[78]. However, no significant differences in LDL-C, HDL-C, or total cholesterol levels were observed between palm oil, olive oil, sunflower oil, or soybean oil enriched diets[77]. It's worth mentioning that palm oil also contains a variety of phytonutrients, including four forms of tocopherols and tocotrienols, carotenoids, sterols, and others. These compounds possess antioxidant activity and are considered beneficial for human health[77,79,80]. Whether and how these compounds contribute to the palm oil-mediated protective effect in the progression of atherosclerosis requires further investigation. Furthermore, additional research is needed to determine if increasing the amount of palmitic acid provides protection against atherosclerosis in other models.

Many of the therapies currently used to treat patients with atherosclerosis and related cardiovascular diseases focus on improving hypertension and lowering blood lipid levels. Our study reveals that HFD-induced LD accumulation in VECs disrupts ciliary homeostasis by reducing cytosolic PA availability, thereby aggravating the progression of atherosclerosis. Therefore, intervention approaches targeting LDs in VECs may represent a potential therapeutic strategy for treating atherosclerosis. Our data demonstrated that mice fed a HFD with palm oil showed improved atherosclerotic compared to those fed a HFD rich in soybean oil. Hence, a further understanding of the effects of specific fatty acid species on vascular endothelial lipid metabolism and the development of atherosclerosis may provide guidance on incorporating dietary interventions to improve the care of patients with atherosclerosis.

Methods

Animals

All mice involved in this study were on a C57BL/6 background. $ApoE^{KO}$ mice were purchased from Beijing Viton Lever Experimental Animal Technology Ltd (Beijing, China). $Ift88^{fl/fl}$ mice, harboring loxP sites flanking exons 4–6 of the *Ift88* gene, were obtained from the Jackson Laboratory (Bar Harbor, ME, USA). Tek-Cre mice were purchased from Cyagen Biosciences (Guangzhou, China). All animals were housed in the animal center of Shandong Normal University under controlled conditions (18–23 °C, 40–60% humidity, 12 h light/dark cycle) and provided with free access to food and water. Male mice were used for this study. Previous reports indicate that atherosclerosis progression is largely similar between genders. Nevertheless, female mice tend to develop larger plaques that are less inflamed compared to those in male mice[81]. Unless otherwise specified, mice were fed a HFD consisting of 1.25% cholesterol, 17% cocoa butter and 3% soybean oil to induce atherosclerosis. Mice were euthanized through cervical dislocation while under general anesthesia induced by the inhalation of isoflurane. All animal procedures were approved by the Animal Ethics Committee of Shandong Normal University.

For experiments to detect the effect of SCD1 inhibitors on atherosclerosis, 8-week-old male mice were fed a HFD for 6 weeks. Then the mice received tail vein injections of A939572 (5 mg/kg body weight) or vehicle every other day for 4 weeks while still on the HFD. Finally, the mice were fasted overnight and euthanized for analysis. For experiments to evaluate the effect of dietary fat content on atherosclerosis, 8-week-old male $ApoE^{KO}$ mice were randomly divided into four groups and were kept on indicated diets for 12 weeks. Compositions of different diets used in this study were described in Supplementary Table 3.

Reagents

OA (O1383), PA (P5585), POA (P9417), SA (S4751), BSA (A1933), 2-BP (21604), palmostatin B (178501), DMSO (D8418), phosphatase inhibitor cocktail (P8340), N-Ethylmaleimide (NEM) (E3876), hydroxylamine (26103), Triton X-100 (T8787), and Oil Red O (O0625) were from Sigma-Aldrich. A922500 (HY-10038), PF-06424439 (HY-108341), Atglistatin (HY-15859), C75 (HY-12364), $^{13}C_{16}$-PA (HY-N0830S6), Cycloheximide (HY-12320), ALA (HY-N0728), and A939572 (HY-50709) were from MCE. BODIPY™ 493/503 (D3922), BODIPY™ FL C16 (D3821), HCS LipidTOX (H34477), DAPI (D3571), Protein A/G Agarose (20421), Streptavidin Agarose beads (88817), and BMCC-Biotin (21900) were purchased from Thermo Fisher. Total cholesterol assay kit (A111-1-1), High-density lipoprotein cholesterol assay kit (A112-1-1), Low-density lipoprotein cholesterol assay kit (A113-1-1), and triglyceride assay kit (A110-1-1) were from Nanjing Jiancheng Bioengineering Institute. EGM-2 medium (CC3156, Lonza), Matrigel (356234, BD Biosciences), Trizol reagent (15596026, Invitrogen), vectamount (H-5501, Vector Lab), SA-β-gal staining kit (C0602, Beyotime), and Fast Green FCF Stain Solution (C500016, Sangon Biotech) were obtained from indicated sources.

Antibodies

Antibodies were obtained and used as specified: rabbit anti-ARL13B (17711-1-AP, ProteinTech; WB 1:3000, IP 3 μg), rabbit anti-RAB8A (55296-1-AP, ProteinTech; WB 1:1000, IP 3 μg), rabbit anti-CEP131 (25735-1-AP, ProteinTech; WB 1:1000, IP 3 μg), rabbit anti-KIF3A (13930-1-AP, ProteinTech; WB 1:1000, IP 3 μg), rabbit anti-PCM1 (19856-1-AP, ProteinTech; WB 1:8000, IP 3 μg), rabbit anti-LC3 (14600-1-AP, ProteinTech; WB 1:2000, IF 1:500), rabbit anti-p16 (10883-1-AP, ProteinTech; WB 1:4000), mouse anti-ac-tubulin (T7451, Sigma-Aldrich; IF 1:1000), rabbit anti-pericentrin (ab220784, Abcam, IF 1:2000), rabbit anti-γ-Tubulin (T3559, Sigma-Aldrich; IF 1:1500), mouse anti-CD31 (ab24590, Abcam; IF 1:1000), rabbit anti-CD31 (MA5-29475, Invitrogen; IF 1:100), mouse anti-VE-cadherin (14-1449-82, Thermo Fisher; IF 1:100), streptavidin HRP (S911, Thermo Fisher), rabbit anti-SCD1 (28678-1-AP, ProteinTech; WB 1:8000), rabbit anti-CHOP (15204-1-AP, ProteinTech; WB 1:1000), rabbit anti-PERK (20582-1-AP, ProteinTech; WB 1:1000), rabbit anti-phospho-PERK (Thr980) (MA5-15033, Thermo Fisher; WB 1:1000), rabbit anti-GAPDH (AB0036, Abways; IB 1:2000), rabbit anti-IgG H+L (Alexa Fluor 568) (ab175471, Abcam; IF 1:1000), mouse anti-IgG H+L (Alexa Fluor 647) (ab150115, Abcam; IF 1:1000), rabbit anti-IgG H+L (Alexa Fluor 647) (ab150075, Abcam; IF 1:1000), mouse anti-IgG H+L (Alexa Fluor 568) (ab175473, Abcam; IF 1:1000), HRP-conjugated goat anti-rabbit IgG (H+L) (SA00001-2, ProteinTech; WB 1:10000), and HRP-conjugated goat anti-mouse IgG (H+L) (SA00001-1, ProteinTech; WB 1:10000).

Atherosclerosis analysis

For whole aorta ORO staining, mice were anesthetized and perfused with 20 mL saline via left ventricular puncture. The heart and entire aorta were isolated and placed in 4% paraformaldehyde (PFA) at 4 °C for at least 24 h for fixation. After removal of adjacent fat and connective tissue, the aorta was opened longitudinally (from the aortic root to the iliac artery bifurcation), stained with ORO for 15 min, and washed with 70% ethanol for 3 min. The aortic tree was pinned to a black rubber plate submerged in PBS and imaged under an Olympus SZX16 stereomicroscope.

For staining of frozen sections of aortic valves, the hearts were sequentially dehydrated with 15% and 30% sucrose at 4 °C and then embedded with optimal cutting temperature compound. A series of 10 μm frozen sections of aortic roots were prepared and processed for ORO staining. Briefly, sections were washed 3 times with PBS and fixed in 4% PFA for 5–10 min, followed by three washes with diH_2O. The sections were then soaked in 60% isopropanol for 5 min, followed by incubation in pre-warmed 0.5% ORO solution for 10 min at 60 °C. Sections were then decolorized in 60% isopropanol solution for 30 s, followed by 3 washes with diH_2O, and incubation in hematoxylin or Fast Green FCF Stain Solution for 30 s. The slides were rinsed 3 times with diH_2O, air-dried, and mounted with coverslips for imaging. Quantification of atherosclerotic lesions was performed using ImageJ (National Institutes of Health).

En face immunofluorescence staining of the aortic arch vascular endothelium

For *En face* immunofluorescence staining of the aortic tissue, mice were perfused with PBS followed by PBS containing 4% PFA after anesthesia. The aortic arches were dissected and fixed in 4% formaldehyde for 30 min, cleaned of fat and connective tissue, and opened longitudinally with microscissors. *En face* preparations were then blocked by incubation with blocking buffer (0.1% Triton X-100, 2% BSA, 1% donkey serum) for 2 h and incubated overnight at 4 °C with primary antibodies. The next day, the samples were washed and incubated for 1 h at room temperature with the corresponding secondary antibodies. Finally, lipid droplets were stained with BODIPY and nucleus were stained with DAPI. The vascular endothelium was then carefully removed and placed on a slide, which was covered and examined using a Leica SP8 confocal microscope.

To determine the fluorescence intensity of LDs and cilia in individual endothelial cells in the mouse aorta, VE-cadherin immunofluorescence staining was performed to label the cell membrane of endothelial cells, allowing us to delineate each cell's region. Using the ImageJ software (National Institutes of Health), we outlined cell regions based on the VE-cadherin fluorescence signal. We then measured the BODIPY fluorescence intensity (LD signal) and the ac-tubulin fluorescence intensity (ciliary signal) within the selected regions using the "measurement" tool (Supplementary Fig. 9). The cultured endothelial cells were segmented and quantified using a similar method as the *en face* aorta imaging.

Serum lipid analyses

Blood samples were collected from mice after 12 h of fasting. Serum was obtained by incubation of blood for 2 h at room temperature, followed by centrifugation (3000 × *g*, 30 min, 4 °C) and freezing at −80 °C for further analyses. The concentrations of triglycerides, high-density lipoprotein cholesterol, low-density lipoprotein cholesterol, and total cholesterol in the serum were determined using colorimetric assays with commercially available kits from Jiancheng Bioengineering Institute, following the manufacturer's protocols.

Isolation of MAECs

MAECs were isolated from the thoracic aortas of mice following previously described protocols[82,83]. Briefly, 2- to 3-month-old mice were anesthetized, and the left ventricle was injected with PBS containing 1000 U/mL heparin to facilitate perfusion of the aorta. The aorta was then dissected from the mice and placed in a Petri dish containing ice-cold PBS. The aorta was carefully washed with ice-cold PBS to remove any surrounding fat tissue. Subsequently, the aorta was transferred to endothelial growth medium and cut into 8–10 small segments using microdissecting scissors. Matrigel was diluted 1:1 with cold DMEM and used to coat a 6-well plate. The aorta segments were placed lumen-side down on the solidified matrix. The aortic explants were cultured in endothelial growth medium at 37 °C. After 4 days, the aortic fragments were removed, and the remaining adherent endothelial cells were further cultured on the substrate for an additional 2–3 days. MAECs were then passaged for subsequent experiments. The isolated MAECs were not authenticated.

Cell culture and treatments

HUVECs (ATCC CRL-1730) and HAECs (ATCC CRL-4052) within five passages were used for experiments. The supplier verified the authenticity of the two cell lines by STR profiling. Cells were cultured in endothelial cell culture medium (EGM-2 BulletKit, Lonza, CC-3162) containing 10% FBS, L-glutamine, and penicillin/streptomycin (P/S). The cells were maintained at 37 °C in a fully humidified incubator with a 95% air and 5% CO_2 atmosphere. To induce cilium formation, cells were cultured in a serum-free medium for 48 h unless stated otherwise. Unless otherwise specified, cells were treated with 200 μM fatty acids for 12 h. For fatty acid conjugation, OA, POA, SA, ALA, and PA were first dissolved in ethanol at 72 °C. Subsequently, they were diluted with a solution of 5% fatty acid-free BSA in PBS, achieving a final concentration of 20 mM. To facilitate the conjugation of fatty acids to BSA, a 10 min incubation at 42 °C was applied.

For GC-MS experiments, HUVECs were treated with 200 μM OA for 12 h or with a DGAT1 inhibitor (A922500, 10 μM) for 24 h, followed by exposure to OA (200 μM) for an additional 12 h (Fig. 3b, c). Additionally, HUVECs were treated as follows: OA (200 μM) for 12 h; DGAT1 overexpression for 48 h; Atglistatin (10 μM) for 24 h; or a DGAT1 inhibitor (A922500, 10 μM) for 24 h, followed by exposure to OA (200 μM) for an additional 12 h (Fig. 3d). For immunofluorescence experiments, HUVECs were treated with DMSO or DGAT inhibitors (A922500, 10 μM and PF-06424439, 5 μM) for 24 h before exposure to BSA or OA (200 μM) for an additional 12 h (Fig. 3e–g). HAECs were treated with DMSO or 50 μM 2-BP for 24 h, exposed to BSA or PA (200 μM) for 12 h, and then serum-starved for 48 h (Fig. 4c, d).

Plasmids and transfections

The coding sequences of human SCD1 and DGAT1 were amplified using KOD-Plus-Neo DNA polymerase (KOD-401, TOYOBO, Shanghai, China). The primers used for SCD1 cloning were as follows: Forward CTAGCGTTTAAACTTAAGCTTATGCCGGCCCACTTGCTG, Reverse CCACACTGGACTAGTGGATCCTCAGCCACTCTTGTAGTTTCCATC. For DGAT1 cloning, the primers were as follows: Forward CTAGCGTTTA AACTTAAGCTTATGGGCGACCGCGGCAGCTC, Reverse CCACACTGG ACTAGTGGATCCTCAGGCCTCTGCCGCTGGGG. After gel extraction, the coding sequence fragments were cloned into the pcDNA3.1 or pCMV-C-EGFP using the Seamless Cloning Kit (C112-01, ClonExpress II One Step Cloning Kit, Vazyme, Nanjing, China). The plasmid encoding Livedrop-mCherry was constructed as reported[84]. DNA sequences encoding ARL13B, ARL13B C8S/C9S, and ARL13B Myr were synthesized by Guangzhou RiboBio and were cloned into corresponding vectors to generate overexpression plasmids for ARL13B-Flag, ARL13B C8S/C9S-Flag, ARL13B-GFP, and ARL13B-GFP Myr. HUVECs and HAECs were transfected using Lipo3000 reagent (Invitrogen, USA), according to the manufacturer's instructions. In general, 6 μL of Lipo3000 reagent and 2 μg of plasmid were diluted into 125 μL of Opti-MEM, respectively, and incubated for 5 min at room temperature, followed by mixing and 20 min of incubation. The mixture was then added to the cells for transfection.

Immunofluorescent staining of cultured cells

Cultured cells were washed twice with PBS and fixed with 4% PFA for 30 min. The cells were then washed three times with PBS. Cell membranes were permeabilized using 0.1% Triton, followed by blocking with 4% BSA for 1 h at room temperature. After that, the cells were incubated overnight at 4 °C with primary antibodies. The next day, the cells were washed and incubated with secondary antibodies for 1 h at room temperature. Finally, the cells were stained with BODIPY and DAPI and observed using a fluorescent microscope. The percentage of ciliated cells was calculated with ImageJ (National Institutes of Health). The fluorescence intensity of lipid droplets was measured using Fiji software (National Institutes of Health).

SA-β-gal staining

An SA-β-gal staining kit (C0602, Beyotime) was used for the identification of senescent cells. Briefly, cultured cells were fixed in a fixative solution for 15 min at room temperature. Then the fixed cells were washed three times with PBS and incubated in a freshly prepared SA-β-gal staining solution at 37 °C overnight. Senescent cells exhibited blue staining when observed under an inverted microscope (Olympus, Japan).

Gas chromatography-mass spectrometry (GC-MS) analysis of fatty acid methyl esters

Cells were grown in 6-well plates to a final density of ≥4 × 10^5 cells/well. Culture medium was removed and cells were washed quickly three times with cold PBS. Serum samples were collected from mice fed with indicated diets ($n = 6$ mice). In brief, dried lipid extracts were resuspended in 300 μL toluene in glass vials and derivatized with 2 mL 5% sulfuric acid in methanol at 95 °C for 1.5 h. After derivatization, 2 mL 0.9% NaCl was added, and the fatty acid methyl esters (FAMEs) were extracted twice with 1 mL hexane. The samples were dried under nitrogen, resuspended in 100 μL hexane, and FAMEs in samples were analyzed by GC-MS. Total ion counts were determined by integrating the appropriate ion fragment for each FAME using El-Maven software (Elucidata). Metabolite data were background corrected using blank samples and normalized to internal standards and biofluid volume/sample weight. Mass isotope distributions were corrected using IsoCorrectoR to obtain natural abundances. Absolute concentrations of fatty acids were calculated based on an external standard curve using the Supelco 37 component FAME mixture.

Isolation of LDs

Isolation of LDs from cultured cells was performed as described previously[85]. Briefly, collected HUVECs were resuspended and homogenized in a buffer containing 20 mM tricine, 250 mM sucrose, and 0.2 mM PMSF (pH 7.8). The LDs were floated by ultracentrifugation at 185,000 × *g* for 2 h. The upper layer LD fraction was then collected and washed three times with a buffer containing 20 mM HEPES, 100 mM

KCl, and 2 mM $MgCl_2$ (pH 7.4). All procedures were performed at 4 °C or on ice.

$^{13}C_{16}$-PA tracing

HUVECs were incubated with 200 μM $^{13}C_{16}$-PA for 24 h, washed with fresh medium, and then exposed to oleic acid treatment, DGAT1 overexpression, or Atglistatin treatment to induce LD formation. Subsequent to these treatments, cytosol and medium fractions were separately collected for the analysis of $^{13}C_{16}$-labeled and total PA, while whole cells and LD fractions were separately obtained for the analysis of $^{13}C_{16}$-labeled and total triglycerides. Three independent samples were collected for each group.

Fatty acid flux analysis was conducted at LipidALL Technologies. Lipids were extracted from cells using 1 mL of ice-cold methanol. Samples were incubated at 1500×*g* for 30 min at 4 °C. At the end of the incubation, samples were centrifuged for 10 min at 12,000×*g* at 4 °C. Clean supernatant was transferred to a new tube and dried in a SpeedVac under OH mode. The dried extract was reconstituted in LCMS grade methanol for fatty acid flux analysis on a system comprising an Agilent 1290 II UPLC coupled to Sciex 5600+ quadrupole-TOF MS. Fatty acids were separated on a Waters ACQUITY HSS-T3 column (3.0 × 100 mm, 1.8 μm). MS parameters for detection were: ESI source voltage negative ion mode −4.5 kV; vaporizer temperature, 500 °C; drying gas (N2) pressure, 50 psi; nebulizer gas (N2) pressure, 50 psi; curtain gas (N2) pressure, 35 psi[86]. Information-dependent acquisition mode was used for MS/MS analyses of the metabolites. Collision energy was set at −35 ± 15 eV. Data acquisition and processing were performed using Analyst® TF 1.7.1 Software (AB Sciex, Concord, ON, Canada). All detected ions were extracted using MarkerView 1.3 (AB Sciex, Concord, ON, Canada) into Excel in the format of two-dimensional matrix, including mass-to-charge ratio (m/z), retention time and peak areas. PeakView 2.2 (AB Sciex, Concord, ON, Canada) was applied to extract MS/MS data and perform comparisons with the Metabolites database (AB Sciex, Concord, ON, Canada), HMDB and standard references to annotate ion identities[87]. 19:0-FFA was used as the internal standard to correct the endogenous metabolites in the samples and normalize them with sample volume.

Untargeted metabolic flux analysis was conducted at LipidALL Technologies. Metabolites were extracted from samples using 400 μL ice-cold methanol: H_2O (v/v 3:1), and were sonicated in bath for 2 min. Next, 1 mL MTBE was added into samples, and incubated at 1500 × *g* for 1 h at room temperature. Then, phase separation was induced by adding 250 μL water, letting it sit for 10 min at room temperature and centrifuging for 15 min at 12,000 × *g*, 4 °C. The two phases, upper organic phase and lower aqueous phase, were separately transferred to fresh tubes. The lower fraction was dried in a SpeedVac under H_2O mode. Total protein content was determined from the dried pellet using the Pierce® BCA Protein Assay Kit according to the manufacturer's protocol. The upper fraction was dried in a SpeedVac under OH mode[6]. The dried extract was reconstituted in 100 μL LCMS grade isopropanol prior to LC-MS analysis on an Agilent 1290 II UPLC coupled to Sciex 5600+ quadrupole-TOF MS. Triglycerides were separated on an Agilent Zorbax Eclipse Plus column (100 × 2.1 mm, 1.8 μm). MS parameters for detection were: ESI source voltage positive ion mode 5.5k V, vaporizer temperature, 500 °C; drying gas (N2) pressure, 50 psi; nebulizer gas (N2) pressure, 50 psi; curtain gas (N2) pressure, 45 psi; The scan range was m/z 200–1000. Information-dependent acquisition mode was used for MS/MS analyses of the metabolites. Collision energy was set at (+) 35 ± 15 eV. Data acquisition and processing were performed using Analyst® TF 1.7.1 Software (AB Sciex, Concord, ON, Canada). All detected ions were extracted using MarkerView 1.3 (AB Sciex, Concord, ON, Canada) into excel in the format of a two-dimensional matrix, including mass-to-charge ratio (m/z), retention time and peak areas. PeakView 2.2 (AB Sciex, Concord, ON, Canada) was applied to extract MS/MS data and perform comparisons with the Metabolites database (AB Sciex, Concord, ON, Canada), HMDB and standard references to annotate ion identities[87]. The protein content was used for the normalization of peak areas.

Acyl-biotin exchange (ABE) palmitoylation assay

For ABE palmitoylation assay, total cell lysates were reductively alkylated with 50 mM N-ethylmaleimide, and proteins were purified using specified antibodies and beads. The purified proteins were divided into two groups, one treated with 1 M hydroxylamine (HAM) and the other with control buffer without HAM, and incubated at room temperature for 1 h. High-affinity streptavidin agarose beads (Thermo; 20 μL bead slurry/200 μg protein) were washed three times. The resuspended samples were then added to the washed beads, which were incubated with rotation at room temperature for 90 min. The beads were then washed with 1% SDS in PBS, resuspended in 1× SDS loading buffer, boiled for 10 min at 95 °C, separated by SDS/PAGE, and analyzed by Western blotting.

Palmitoylation modification proteomic analysis

HUVECs treated with 200 μM OA or BSA for 12 h were washed three times with cold PBS and then collected ($n = 1$ for each group). Palmitoylation modification proteomic analysis was carried out at AlMSMASS Co., Ltd. (Shanghai, China). The preparation protocol is as follows: Cells were lysed, centrifuged at 4500 × *g* for 10 min at 4 °C, and the supernatant was collected. Chloroform-methanol precipitation was performed on the protein sample, followed by centrifugation and air drying of the precipitate. The precipitate was then resuspended in 4% SDS buffer and NEM, and incubated at 37 °C. Free thiols were blocked with lysis buffer (LB) containing 1 mM NEM, 1 mM PMSF, 1× PI, and 0.2% Triton X-100 at 4 °C overnight. Residual NEM was removed with three chloroform-methanol (CM) precipitations, with the precipitate being dissolved each time. Samples were treated with hydroxylamine (HA) for the experimental group and buffer without HA for the control group. The samples were labeled with Biotin-HPDP buffer, followed by three CM precipitations, and then diluted. Protein samples were bound to streptavidin agarose beads, incubated, and washed with LB containing SDS and Triton X-100. The target protein was eluted, incubated at 37 °C, centrifuged, and the supernatant was collected. The solution was thawed at 4 °C, centrifuged, and the supernatant was collected for reductive alkylation. Trypsin was added at a 50:1 ratio of protein to enzyme and digested at 37 °C for over 16 h. After desalting and purification, the sample was vacuum-concentrated and dried.

Samples were analyzed using liquid chromatography-tandem mass spectrometry (LC-MS/MS) with an EASY-nLC 1000 ultra-performance liquid chromatography (UPLC) system connected to an LTQ Velos mass spectrometer (Thermo Fisher Scientific). Twenty microliters of peptide solution were separated on a 15 cm analytical column using a 140 min LC gradient at a flow rate of 300 nL/min. Mass spectra were acquired in a data-dependent manner with automatic switching between MS and MS/MS scans. Full scans were performed with a resolution of 60,000 at m/z 400. Up to 20 of the most intense peptide ions with a charge state of ≥2 were automatically selected for MS/MS fragmentation, either by collision-induced dissociation (CID) or electron transfer dissociation (ETD). Dynamic exclusion was enabled with a repeat count of 1, an exclusion duration of 30 s, and a repeat duration of 30 s. The acquired MS data (10 RAW files) were searched against the Uniprot Human database (released on September 11, 2012, containing 84,680 sequences) using MaxQuant (v1.3.0.5). The search parameters were as follows: trypsin/P as the protease; oxidation (M), acetylation (protein N-term), N-ethylmaleimide (NEM, C), and carbamidomethylation (C) as variable modifications; up to two missed

cleavages; minimum peptide length as 7; identification of second peptides enabled; mass tolerance for MS1 set at 20 ppm and for MS2 set at 0.7 Da. A stringent 1% false discovery rate (FDR) was applied to filter peptide spectrum matches (PSMs), peptide, and protein identifications.

Western blotting

Cultured cells were lysed using RIPA lysis buffer (P0013, Beyotime, Shanghai, China) containing protease inhibitors. Using 10% Bis-tris polyacrylamide gel electrophoresis, proteins were separated and transferred to polyvinylidene difluoride membranes. The blots were then blocked in 5% skim milk at room temperature for 2 h before being incubated overnight at 4 °C with primary antibodies. After three washes, the membranes were incubated for 1 h with the corresponding secondary antibodies. The protein bands on the membranes were detected by ECL Western blot reagents (WBULS0100, Millipore). The intensity of the immunoblots was measured by densitometry using ImageJ.

Quantitative real-time PCR

Total RNA was extracted from cultured cells or tissue samples using Trizol reagent (15596026, Invitrogen). 1 μg of RNA was reverse transcribed using the PrimeScriptTM RT kit with gDNA Eraser (Takara, Otsu, Japan) according to the manufacturer's instructions. The cDNA was amplified using EXPRESS SYBR GreenER with premixed ROX (11794200, Invitrogen). The primers used for PCR are listed in Supplementary Table 4. Relative mRNA expression levels were normalized to the level of GAPDH.

Statistical analysis

The results were presented as mean ± SEM unless indicated otherwise. All data were collected from at least three independent experiments unless indicated otherwise. Group comparisons were analyzed using unpaired two-tailed Student's *t*-test or one/two-way ANOVA analysis with post hoc analysis. All data analyses were performed using GraphPad Prism v.8.0.1 software.

Reporting summary

Further information on research design is available in the Nature Portfolio Reporting Summary linked to this article.

Data availability

Mass spectrometry raw data generated in this study have been deposited to the ProteomeXchange (http://proteomecentral.proteomexchange.org) via the PRIDE partner repository with the dataset identifier PXD052827. All other relevant data supporting the key findings of this study are available within the article, its Supplementary Information, or from the corresponding authors upon request. Source data are provided in the Source Data file. Source data are provided with this paper.

References

1. Shi, L. et al. Brown adipose tissue-derived Nrg4 alleviates endothelial inflammation and atherosclerosis in male mice. *Nat. Metab.* **4**, 1573–1590 (2022).
2. Liu, M. et al. Macrophage K63-linked ubiquitination of YAP promotes its nuclear localization and exacerbates atherosclerosis. *Cell Rep.* **32**, 107990 (2020).
3. Karunakaran, D. et al. RIPK1 expression associates with inflammation in early atherosclerosis in humans and can be therapeutically silenced to reduce NF-κB activation and atherogenesis in mice. *Circulation* **143**, 163–177 (2021).
4. Ma, H. et al. NuMA forms condensates through phase separation to drive spindle pole assembly. *J. Mol. Cell Biol.* **14**, mjab081 (2022).
5. Jia, M. et al. Deletion of BACH1 attenuates atherosclerosis by reducing endothelial inflammation. *Circ. Res.* **130**, 1038–1055 (2022).
6. Lam, S. M. et al. A multi-omics investigation of the composition and function of extracellular vesicles along the temporal trajectory of COVID-19. *Nat. Metab.* **3**, 909–922 (2021).
7. Yang, Q. et al. PRKAA1/AMPKα1-driven glycolysis in endothelial cells exposed to disturbed flow protects against atherosclerosis. *Nat. Commun.* **9**, 4667 (2018).
8. Dinsmore, C. & Reiter, J. F. Endothelial primary cilia inhibit atherosclerosis. *EMBO Rep.* **17**, 156–166 (2016).
9. Ran, J. & Zhou, J. Targeting the photoreceptor cilium for the treatment of retinal diseases. *Acta Pharm. Sin.* **41**, 1410–1415 (2020).
10. Ran, J. et al. ASK1-mediated phosphorylation blocks HDAC6 ubiquitination and degradation to drive the disassembly of photoreceptor connecting cilia. *Dev. Cell* **53**, 287–299.e285 (2020).
11. Ran, J. et al. Targeting the HDAC6-cilium axis ameliorates the pathological changes associated with retinopathy of prematurity. *Adv. Sci.* **9**, e2105365 (2022).
12. Gupta, A. et al. Cilia proteins are biomarkers of altered flow in the vasculature. *JCI Insight* **7**, e151813 (2022).
13. Hierck, B. P. et al. Primary cilia sensitize endothelial cells for fluid shear stress. *Dev. Dyn.* **237**, 725–735 (2008).
14. Guo, J. et al. Primary cilia signaling shapes the development of interneuronal connectivity. *Dev. Cell* **42**, 286–300.e284 (2017).
15. Yang, Y. et al. A cilium-independent role for intraflagellar transport 88 in regulating angiogenesis. *Sci. Bull.* **66**, 727–739 (2021).
16. Qi, F. & Zhou, J. Multifaceted roles of centrosomes in development, health, and disease. *J. Mol. Cell Biol.* **13**, 611–621 (2021).
17. Egorova, A. D. et al. Lack of primary cilia primes shear-induced endothelial-to-mesenchymal transition. *Circ. Res.* **108**, 1093–1101 (2011).
18. Luu, V. Z., Chowdhury, B., Al-Omran, M., Hess, D. A. & Verma, S. Role of endothelial primary cilia as fluid mechanosensors on vascular health. *Atherosclerosis* **275**, 196–204 (2018).
19. Xie, W. et al. The tumor suppressor CYLD controls epithelial morphogenesis and homeostasis by regulating mitotic spindle behavior and adherens junction assembly. *J. Genet. Genomics* **44**, 343–353 (2017).
20. Xie, W. et al. HIV-1 exposure triggers autophagic degradation of stathmin and hyperstabilization of microtubules to disrupt epithelial cell junctions. *Signal Transduct. Target. Ther.* **5**, 79 (2020).
21. Kuo, A., Lee, M. Y. & Sessa, W. C. Lipid droplet biogenesis and function in the endothelium. *Circ. Res.* **120**, 1289–1297 (2017).
22. Kuo, A., Lee, M. Y., Yang, K., Gross, R. W. & Sessa, W. C. Caveolin-1 regulates lipid droplet metabolism in endothelial cells via autocrine prostacyclin-stimulated, cAMP-mediated lipolysis. *J. Biol. Chem.* **293**, 973–983 (2018).
23. Wilfling, F. et al. Triacylglycerol synthesis enzymes mediate lipid droplet growth by relocalizing from the ER to lipid droplets. *Dev. Cell* **24**, 384–399 (2013).
24. Wu, Y., Zhou, J. & Yang, Y. Peripheral and central control of obesity by primary cilia. *J. Genet. Genomics* **50**, 295–304 (2023).
25. Nguyen, T. B. et al. DGAT1-dependent lipid droplet biogenesis protects mitochondrial function during starvation-induced autophagy. *Dev. Cell* **42**, 9–21.e25 (2017).
26. Walther, T. C., Chung, J. & Farese, R. V. Jr Lipid droplet biogenesis. *Annu. Rev. Cell Dev. Biol.* **33**, 491–510 (2017).
27. Olzmann, J. A. & Carvalho, P. Dynamics and functions of lipid droplets. *Nat. Rev. Mol. Cell Biol.* **20**, 137–155 (2019).
28. Lien, E. C. et al. Low glycaemic diets alter lipid metabolism to influence tumour growth. *Nature* **599**, 302–307 (2021).
29. Vivas-Garcia, Y. et al. Lineage-restricted regulation of SCD and fatty acid saturation by MITF controls melanoma phenotypic plasticity. *Mol. Cell* **77**, 120–137.e129 (2020).

30. Xuan, Y. et al. SCD1/FADS2 fatty acid desaturases equipoise lipid metabolic activity and redox-driven ferroptosis in ascites-derived ovarian cancer cells. *Theranostics* **12**, 3534–3552 (2022).
31. Savransky, V. et al. Dyslipidemia and atherosclerosis induced by chronic intermittent hypoxia are attenuated by deficiency of stearoyl coenzyme A desaturase. *Circ. Res.* **103**, 1173–1180 (2008).
32. Brown, J. M. et al. Inhibition of stearoyl-coenzyme A desaturase 1 dissociates insulin resistance and obesity from atherosclerosis. *Circulation* **118**, 1467–1475 (2008).
33. Romanauska, A. & Kohler, A. Reprogrammed lipid metabolism protects inner nuclear membrane against unsaturated fat. *Dev. Cell* **56**, 2562–2578.e2563 (2021).
34. Mei, S. et al. Differential roles of unsaturated and saturated fatty acids on autophagy and apoptosis in hepatocytes. *J. Pharm. Exp. Ther.* **339**, 487–498 (2011).
35. Eynaudi, A. et al. Differential effects of oleic and palmitic acids on lipid droplet-mitochondria interaction in the hepatic cell line HepG2. *Front. Nutr.* **8**, 775382 (2021).
36. Wang, H. et al. Seipin is required for converting nascent to mature lipid droplets. *Elife* **5**, e16582 (2016).
37. Avalos, Y. et al. Palmitic acid control of ciliogenesis modulates insulin signaling in hypothalamic neurons through an autophagy-dependent mechanism. *Cell Death Dis.* **13**, 659 (2022).
38. Ge, X. et al. Protein palmitoylation-mediated palmitic acid sensing causes blood-testis barrier damage via inducing ER stress. *Redox Biol.* **54**, 102380 (2022).
39. Roy, K. & Marin, E. P. Lipid modifications in cilia biology. *J. Clin. Med.* **8**, 921 (2019).
40. Bay, S. N., Long, A. B. & Caspary, T. Disruption of the ciliary GTPase Arl13b suppresses Sonic hedgehog overactivation and inhibits medulloblastoma formation. *Proc. Natl Acad. Sci. USA* **115**, 1570–1575 (2018).
41. Li, Y. et al. Deletion of ADP ribosylation factor-like GTPase 13B leads to kidney cysts. *J. Am. Soc. Nephrol.* **27**, 3628–3638 (2016).
42. Ran, J. et al. A non-mitotic role for Eg5 in regulating cilium formation and sonic hedgehog signaling. *Sci. Bull.* **66**, 1620–1623 (2021).
43. Roy, K. et al. Palmitoylation of the ciliary GTPase ARL13b is necessary for its stability and its role in cilia formation. *J. Biol. Chem.* **292**, 17703–17717 (2017).
44. Hao, J. W. et al. CD36 facilitates fatty acid uptake by dynamic palmitoylation-regulated endocytosis. *Nat. Commun.* **11**, 4765 (2020).
45. Shi, C. et al. ZDHHC18 negatively regulates cGAS-mediated innate immunity through palmitoylation. *EMBO J.* **41**, e109272 (2022).
46. Nasr, M. et al. PI3KCIIα-dependent autophagy program protects from endothelial dysfunction and atherosclerosis in response to low shear stress in mice. *Arterioscler. Thromb. Vasc. Biol.* **44**, 620–634 (2024).
47. Zhan, W., Tian, W., Zhang, W., Tian, H. & Sun, T. ANGPTL4 attenuates palmitic acid-induced endothelial cell injury by increasing autophagy. *Cell Signal* **98**, 110410 (2022).
48. Xiao, X. T. et al. Green tea polyphenols prevent early vascular aging induced by high-fat diet via promoting autophagy in young adult rats. *Curr. Med. Sci.* **42**, 981–990 (2022).
49. Brophy, M. L. et al. Myeloid-specific deletion of epsins 1 and 2 reduces atherosclerosis by preventing LRP-1 downregulation. *Circ. Res.* **124**, e6–e19 (2019).
50. Gimbrone, M. A. Jr. & Garcia-Cardena, G. Endothelial cell dysfunction and the pathobiology of atherosclerosis. *Circ. Res.* **118**, 620–636 (2016).
51. Kim, B. et al. Endothelial lipid droplets suppress eNOS to link high fat consumption to blood pressure elevation. *J. Clin. Invest.* **133**, e173160 (2023).
52. Boutagy, N. E. et al. Dynamic metabolism of endothelial triglycerides protects against atherosclerosis in mice. *J. Clin. Invest.* **134**, e170453 (2024).
53. Van der Heiden, K. et al. Endothelial primary cilia in areas of disturbed flow are at the base of atherosclerosis. *Atherosclerosis* **196**, 542–550 (2008).
54. Iomini, C., Tejada, K., Mo, W., Vaananen, H. & Piperno, G. Primary cilia of human endothelial cells disassemble under laminar shear stress. *J. Cell Biol.* **164**, 811–817 (2004).
55. Wang, Z. M., Gao, X. F., Zhang, J. J. & Chen, S. L. Primary cilia and atherosclerosis. *Front. Physiol.* **12**, 640774 (2021).
56. Hilgendorf, K. I. et al. Omega-3 fatty acids activate ciliary FFAR4 to control adipogenesis. *Cell* **179**, 1289–1305.e1221 (2019).
57. Chen, J. et al. Deletion of kif3a in CK19 positive cells leads to primary cilia loss, biliary cell proliferation and cystic liver lesions in TAA-treated mice. *Biochim. Biophys. Acta Mol. Basis Dis.* **1868**, 166335 (2022).
58. Nosavanh, L. et al. Cell-autonomous activation of Hedgehog signaling inhibits brown adipose tissue development. *Proc. Natl Acad. Sci. USA* **112**, 5069–5074 (2015).
59. Toomey, M. B. & Corbo, J. C. Evolution, development and function of vertebrate cone oil droplets. *Front. Neural Circuits* **11**, 97 (2017).
60. Muszbek, L., Haramura, G., Cluette-Brown, J. E., Van Cott, E. M. & Laposata, M. The pool of fatty acids covalently bound to platelet proteins by thioester linkages can be altered by exogenously supplied fatty acids. *Lipids* **34**, S331–S337 (1999).
61. Zhang, X. et al. Notum is required for neural and head induction via Wnt deacylation, oxidation, and inactivation. *Dev. Cell* **32**, 719–730 (2015).
62. Liu, Y. et al. Mechanisms and inhibition of Porcupine-mediated Wnt acylation. *Nature* **607**, 816–822 (2022).
63. Nachury, M. V. et al. A core complex of BBS proteins cooperates with the GTPase Rab8 to promote ciliary membrane biogenesis. *Cell* **129**, 1201–1213 (2007).
64. Wilkinson, C. J., Carl, M. & Harris, W. A. Cep70 and Cep131 contribute to ciliogenesis in zebrafish embryos. *BMC Cell Biol.* **10**, 17 (2009).
65. Segal-Salto, M. et al. Proteomics insights into infantile neuronal ceroid lipofuscinosis (CLN1) point to the involvement of cilia pathology in the disease. *Hum. Mol. Genet.* **26**, 1678 (2017).
66. Luis, G. et al. Tumor resistance to ferroptosis driven by stearoyl-CoA desaturase-1 (SCD1) in cancer cells and fatty acid biding protein-4 (FABP4) in tumor microenvironment promote tumor recurrence. *Redox Biol.* **43**, 102006 (2021).
67. Li, F. et al. Lipidomics reveals a link between CYP1B1 and SCD1 in promoting obesity. *J. Proteome Res.* **13**, 2679–2687 (2014).
68. Singh, V. et al. Microbiota-dependent hepatic lipogenesis mediated by stearoyl CoA desaturase 1 (SCD1) promotes metabolic syndrome in TLR5-deficient mice. *Cell Metab.* **22**, 983–996 (2015).
69. MacDonald, M. L. et al. Despite antiatherogenic metabolic characteristics, SCD1-deficient mice have increased inflammation and atherosclerosis. *Arterioscler. Thromb. Vasc. Biol.* **29**, 341–347 (2009).
70. Peter, A. et al. Induction of stearoyl-CoA desaturase protects human arterial endothelial cells against lipotoxicity. *Am. J. Physiol. Endocrinol. Metab.* **295**, E339–349, (2008).
71. Qin, X. et al. Laminar shear stress up-regulates the expression of stearoyl-CoA desaturase-1 in vascular endothelial cells. *Cardiovasc. Res.* **74**, 506–514 (2007).
72. Cavallero, S. et al. Exercise mitigates flow recirculation and activates metabolic transducer SCD1 to catalyze vascular protective metabolites. *Sci. Adv.* **10**, eadj7481 (2024).
73. Katoh, Y. et al. Inhibition of stearoyl-CoA desaturase 1 (SCD1) enhances the antitumor T cell response through regulating beta-catenin signaling in cancer cells and ER stress in T cells and

synergizes with anti-PD-1 antibody. *J. Immunother. Cancer* **10**, e004616 (2022).
74. von Roemeling, C. A. et al. Stearoyl-CoA desaturase 1 is a novel molecular therapeutic target for clear cell renal cell carcinoma. *Clin. Cancer Res.* **19**, 2368–2380 (2013).
75. Zhang, Y. et al. Stearoyl-CoA desaturase-1 dependent lipid droplets accumulation in cancer-associated fibroblasts facilitates the progression of lung cancer. *Int. J. Biol. Sci.* **18**, 6114–6128 (2022).
76. Loganathan, R., Subramaniam, K. M., Radhakrishnan, A. K., Choo, Y. M. & Teng, K. T. Health-promoting effects of red palm oil: evidence from animal and human studies. *Nutr. Rev.* **75**, 98–113 (2017).
77. Medvedev, O. S. & Medvedeva, N. A. Modern conceptions about the possible impact of palm oil on human health. *Vopr. Pitan.* **85**, 5–18 (2016).
78. Li, F., Tan, W., Kang, Z. & Wong, C. W. Tocotrienol enriched palm oil prevents atherosclerosis through modulating the activities of peroxisome proliferators-activated receptors. *Atherosclerosis* **211**, 278–282 (2010).
79. Zainal, Z., Khaza'ai, H., Kutty Radhakrishnan, A. & Chang, S. K. Therapeutic potential of palm oil vitamin E-derived tocotrienols in inflammation and chronic diseases: evidence from preclinical and clinical studies. *Food Res. Int.* **156**, 111175 (2022).
80. Hassan, N. S. M. et al. Influence of fresh palm fruit sterilization in the production of carotenoid-rich virgin palm oil. *Foods* **10**, 2838 (2021).
81. Man, J. J., Beckman, J. A. & Jaffe, I. Z. Sex as a biological variable in atherosclerosis. *Circ. Res.* **126**, 1297–1319 (2020).
82. Hsu, P. L., Chen, J. S., Wang, C. Y., Wu, H. L. & Mo, F. E. Shear-induced CCN1 promotes atheroprone endothelial phenotypes and atherosclerosis. *Circulation* **139**, 2877–2891 (2019).
83. Wang, J. M., Chen, A. F. & Zhang, K. Isolation and primary culture of mouse aortic endothelial cells. *J. Vis. Exp.* **118**, e52965 (2016).
84. Olarte, M. J. et al. Determinants of endoplasmic reticulum-to-lipid droplet protein targeting. *Dev. Cell* **54**, 471–487.e477 (2020).
85. Ding, Y. et al. Isolating lipid droplets from multiple species. *Nat. Protoc.* **8**, 43–51 (2013).
86. Song, J. W. et al. Omics-driven systems interrogation of metabolic dysregulation in COVID-19 pathogenesis. *Cell Metab.* **32**, 188–202.e185 (2020).
87. Tian, H. et al. Precise metabolomics reveals a diversity of aging-associated metabolic features. *Small Methods* **6**, e2200130 (2022).

Acknowledgements

This work was supported by the National Key R&D Program of China (2022YFA0807100 to Y.Y.), the National Natural Science Foundation of China (31991193 to J.Z. and 32100948 to Y.Y.), and the Natural Science Foundation of Shandong Province (2022HWTQ-024 and ZR2021QC026 to Y.Y., and ZR2023QC058 to Y.T.).

Author contributions

Jun Zhou and Yunfan Yang supervised the project. Yanjie Tan, Jun Zhou, and Yunfan Yang designed the experiments. Yanjie Tan, Zhenzhou Huang, Yi Jin, Jiaying Wang, Hongjun Fan, Yangyang Liu, Liang Zhang, Yue Wu, Peiwei Liu, Tianliang Li, Jie Ran, He Tian, Sin Man Lam, and Min Liu performed the experiments. Yanjie Tan and Zhenzhou Huang analyzed the data. Yanjie Tan, Jun Zhou, and Yunfan Yang wrote the manuscript.

Competing interests

The authors declare no competing interests.

Additional information

Supplementary information The online version contains supplementary material available at https://doi.org/10.1038/s41467-024-52621-x.

Correspondence and requests for materials should be addressed to Jun Zhou or Yunfan Yang.

Peer review information *Nature Communications* thanks Muriel Laffargue and the other anonymous reviewer(s) for their contribution to the peer review of this work. A peer review file is available.